The Astrophysical Journal, 834:104 (19pp), 2017 January 10 doi:10.3847/1538-4357/834/2/104

THE 2015 DECAY OF THE BLACK HOLE X-RAY BINARY V404 CYGNI: ROBUST DISK-JET COUPLING AND A SHARP TRANSITION INTO QUIESCENCE

R. M. Plotkin[1], J. C. A. Miller-Jones[1], E. Gallo[2], P. G. Jonker[3,4], J. Homan[5], J. A. Tomsick[6], P. Kaaret[7], D. M. Russell[8], S. Heinz[9], E. J. Hodges-Kluck[2], S. Markoff[10], G. R. Sivakoff[11], D. Altamirano[12], and J. Neilsen[5,13]
[1] International Centre for Radio Astronomy Research—Curtin University, GPO Box U1987, Perth, WA 6845, Australia; richard.plotkin@curtin.edu.au
[2] Department of Astronomy, University of Michigan, 1085 South University Avenue, Ann Arbor, MI 48109, USA
[3] SRON, Netherlands Institute for Space Research, Sorbonnelaan 2, NL-3584 CA Utrecht, The Netherlands
[4] Department of Astrophysics/IMAPP, Radboud University, P.O. Box 9010, 6500 GL Nijmegen, The Netherlands
[5] MIT Kavli Institute for Astrophysics and Space Research, 77 Massachusetts Avenue 37-582D, Cambridge, MA 02139, USA
[6] Space Sciences Laboratory, 7 Gauss Way, University of California, Berkeley, CA 94720-7450, USA
[7] Department of Physics and Astronomy, University of Iowa, Iowa City, IA 52242, USA
[8] New York University Abu Dhabi, P.O. Box 129188, Abu Dhabi, UAE
[9] Department of Astronomy, University of Wisconsin-Madison, Madison, WI 53706, USA
[10] Anton Pannekoek Institute for Astronomy, University of Amsterdam, 1098 XH Amsterdam, The Netherlands
[11] Department of Physics, University of Alberta, 4-181 CCIS, Edmonton, AB T6G 2E1, Canada
[12] Department of Physics and Astronomy, University of Southampton, Highfield SO17 IBJ, UK
Received 2016 September 14; revised 2016 October 25; accepted 2016 November 3; published 2017 January 5

ABSTRACT

We present simultaneous X-ray and radio observations of the black hole X-ray binary V404 Cygni at the end of its 2015 outburst. From 2015 July 11–August 5, we monitored V404 Cygni with *Chandra*, *Swift*, and *NuSTAR* in the X-ray, and with the Karl G. Jansky Very Large Array and the Very Long Baseline Array in the radio, spanning a range of luminosities that were poorly covered during its previous outburst in 1989 (our 2015 campaign covers $2 \times 10^{33} \lesssim L_X \lesssim 10^{34}$ erg s^{-1}). During our 2015 campaign, the X-ray spectrum evolved rapidly from a hard photon index of $\Gamma \approx 1.6$ (at $L_X \approx 10^{34}$ erg s^{-1}) to a softer $\Gamma \approx 2$ (at $L_X \approx 3 \times 10^{33}$ erg s^{-1}). We argue that V404 Cygni reaching $\Gamma \approx 2$ marks the beginning of the quiescent spectral state, which occurs at a factor of ≈3–4 higher X-ray luminosity than the average pre-outburst luminosity of $\approx 8 \times 10^{32}$ erg s^{-1}. V404 Cygni falls along the same radio/X-ray luminosity correlation that it followed during its previous outburst in 1989, implying a robust disk-jet coupling. We exclude the possibility that a synchrotron-cooled jet dominates the X-ray emission in quiescence, leaving synchrotron self-Compton from either a hot accretion flow or from a radiatively cooled jet as the most likely sources of X-ray radiation, and/or particle acceleration along the jet becoming less efficient in quiescence. Finally, we present the first indications of correlated radio and X-ray variability on minute timescales in quiescence, tentatively measuring the radio emission to lag the X-ray by 15 ± 4 minute, suggestive of X-ray variations propagating down a jet with a length of <3.0 au.

Key words: accretion, accretion disks – stars: black holes – stars: individual (V404 Cygni) – X-rays: binaries

1. INTRODUCTION

After spending 26 years in quiescence, the low-mass black hole X-ray binary (BHXB) V404 Cygni was detected in outburst on 2015 June 15 (Barthelmy et al. 2015; Kuulkers et al. 2015; Negoro et al. 2015; Younes 2015), prompting an array of multiwavelength observations. For about two weeks, V404 Cygni displayed spectacular variability from the radio through the gamma-ray (e.g., Mooley et al. 2015; Motta et al. 2015; Rodriguez et al. 2015; Roques et al. 2015; Tetarenko et al. 2015b; Trushkin et al. 2015; Gandhi et al. 2016; Jenke et al. 2016; Kimura et al. 2016; Martí et al. 2016; Walton et al. 2016), while also launching powerful outflows in the form of ballistic synchrotron jets (Tetarenko et al. 2015c) and fast disk winds (King et al. 2015; Muñoz-Darias et al. 2016). During these two weeks, V404 Cygni also contained a high column of absorbing material ($\approx 10^{24}$ cm^{-2}), likely caused by material expelled from the accretion disk obscuring the central engine (Motta et al. 2016). On 2015 June 26, V404 Cygni exhibited the brightest X-ray flare of the outburst, which was followed by a sudden decrease in flux (Sanchez-Fernandez et al. 2016), and the source began a gradual decay back toward quiescence at all wavebands (e.g., Ferrigno et al. 2015; Martin-Carrillo et al. 2015; Tetarenko et al. 2015a; Walton et al. 2015). The high column density during the initial two weeks dissipated and approached the pre-outburst value of $\approx 10^{22}$ cm^{-2} by 2015 July 2–5 (Sivakoff et al. 2015a).

This paper focuses on simultaneous X-ray and radio monitoring of the tail end of the decay, from 2015 July 11—August 5. V404 Cygni is one of our prime laboratories for testing models of accretion physics against observations, largely because it is a nearby BHXB with an accurate distance of 2.39 ± 0.14 kpc measured from radio parallax (Miller-Jones et al. 2009), allowing precise calculations of its energetics. Furthermore, its orbital parameters are well-determined, with the system comprised of a $9.0^{+0.2}_{-0.6}\,M_\odot$ black hole and a K3 III companion star (Khargharia et al. 2010) in a 6.473 ± 0.001 d orbit (Casares et al. 1992), with an inclination of 67^{+3}_{-1} deg (Khargharia et al. 2010).

During a typical outburst, BHXBs begin their final descent while in the "low-hard state" ($L_X \lesssim 10^{-2}\,L_{Edd}$; for V404 Cygni, the Eddington luminosity $L_{Edd} = 1.13 \times 10^{39}$ erg s^{-1}), where their X-ray spectra can be described by a power law with a photon index[14] of $\Gamma \approx 1.6$–1.7 (see, e.g., Remillard &

[13] Hubble Postdoctoral Fellow.

[14] The photon index Γ is defined such that the photon number density N_E (per unit photon energy E) follows $N_E \propto E^{-\Gamma}$.

McClintock 2006; Belloni 2010, for reviews on BHXB spectral states). In the low-hard state, the inner regions of the disk are under-luminous because material is unable to efficiently cool via radiative losses (e.g., Ichimaru 1977; Narayan & Yi 1994; Abramowicz et al. 1995; Yuan & Narayan 2014), resulting in a hot, geometrically thick, radiatively inefficient accretion flow (RIAF), which is likely to develop outflows (e.g., Narayan & Yi 1995; Blandford & Begelman 1999). Compact radio emission is nearly always associated with low-hard state BHXBs, which is usually interpreted as optically thick synchrotron radiation from partially self-absorbed relativistic jets (e.g., Blandford & Königl 1979; Hjellming & Johnston 1988; Fender 2001), and these jets may carry away a substantial fraction of the accretion power (e.g., Fender et al. 2003). Finally, there is evidence that a cool, thin disk (e.g., Shakura & Sunyaev 1973) can persist close to the innermost stable circular orbit toward the bright end of the low-hard state (Miller et al. 2006; Reis et al. 2010; Uttley et al. 2011), but the disk is observed to recede at lower luminosities (see, e.g., Tomsick et al. 2009).

As BHXBs fade from the low-hard state toward quiescence, their X-ray spectra become softer (e.g., Tomsick et al. 2001, 2004; Kalemci et al. 2005; Wu & Gu 2008; Sobolewska et al. 2011; Armas Padilla et al. 2013) until they display $\Gamma \approx 2.1$ (e.g., Kong et al. 2002; Corbel et al. 2006; Plotkin et al. 2013; Armas Padilla et al. 2014; Reynolds et al. 2014; Yang et al. 2015). From an ensemble of quiescent BHXBs, Plotkin et al. (2013) argue that the X-ray spectral softening completes by $10^{-5}\,L_{\rm Edd}$, at which point the X-ray spectral shape remains constant as BHXBs continue to fade (also see Sobolewska et al. 2011). However, the cause of the softening remains unclear, largely because observations with sufficient sensitivity and cadence to track the photon index as it approaches, reaches, and eventually saturates to $\Gamma \approx 2.1$ are scarce (see, e.g., Kalemci et al. 2005; Homan et al. 2013 for examples of some of the best covered decays so far).

Combining X-ray spectral information with radio observations can yield insight into the cause of the X-ray spectral softening, and how BHXBs may differ between quiescence and the low-hard state. During the decay toward quiescence, hard-state BHXBs display correlated X-ray and radio variations on day to week timescales, such that individual systems travel along non-arbitrary paths through the radio/X-ray luminosity plane (Corbel et al. 2013; Gallo et al. 2014). These correlations are taken as evidence for couplings between the inner accretion flow (probed by X-rays) and the compact jet (probed by the radio), and the slope of radio/X-ray luminosity correlations places constraints on the physical mechanisms responsible for the observed radiation (e.g., Heinz & Sunyaev 2003; Markoff et al. 2003). However, even among the systems with the best multiwavelength coverage of the decay toward quiescence (Jonker et al. 2010, 2012; Ratti et al. 2012), none of them also contain high-quality spectral information around the key parameter space of $L_{\rm X} \approx 10^{-5}\,L_{\rm Edd}$, and it is observationally unclear how any motion through the radio/X-ray plane connects to changes in the X-ray spectrum.

The 2015 outburst of V404 Cygni offered a unique opportunity to obtain sensitive X-ray and radio spectral observations of a BHXB around $L_{\rm X} \approx 10^{-5}\,L_{\rm Edd}$ as it transitions into quiescence. Using primarily *Chandra*, *Swift*, and the Karl G. Jansky Very Large Array (VLA), we obtained simultaneous X-ray and radio monitoring observations over three weeks. Of key importance is the relatively small distance to V404 Cygni, which allows high signal-to-noise ratio (S/N) observations at the desired luminosities. Also, the long-orbital period of V404 Cygni implies a large accretion disk and high-mass transfer rate from the companion star (Menou et al. 1999, and references therein), such that, when not in outburst, V404 Cygni has the highest luminosity of any known BHXB with a well-determined distance ($L_{\rm X} \approx 10^{33}\,{\rm erg\,s^{-1}}$; Bernardini & Cackett 2014; an exception is the anomalously luminous, but distant, BHXB GS 1354 − 64; Reynolds & Miller 2011). Thus, V404 Cygni is arguably the best-studied quiescent BHXB (e.g., Casares et al. 1992; Shahbaz et al. 1994; Narayan et al. 1997; Hynes et al. 2004, 2009; Miller-Jones et al. 2008; Bernardini & Cackett 2014; Xie et al. 2014; Markoff et al. 2015; Bernardini et al. 2016a; Rana et al. 2016), thereby allowing rich comparisons between our observations and its pre-outburst properties.

In Section 2, we describe our observations and data reduction. We present results in Section 3, which are discussed in Section 4. During its 26 years of quiescence between outbursts, V404 Cygni displayed strong X-ray variability by up to a factor of five to eight over its average X-ray flux (0.5–10 keV) of $1.2 \pm 0.3 \times 10^{12}\,{\rm erg\,s^{-1}\,cm^{-2}}$ (corresponding to $L_{\rm X} = 8 \times 10^{32}\,{\rm erg\,s^{-1}} = 10^{-6.2}\,L_{\rm Edd}$; Bernardini & Cackett 2014, note that we convert their reported 0.3–10 keV values to 0.5–10 keV here). Throughout the paper, we refer to the above as the "pre-outburst" flux of V404 Cygni. At the beginning of Section 4, we argue that V404 Cygni enters the quiescent spectral state at three to four times higher luminosity. Therefore, throughout the paper, we define quiescence for V404 Cygni to correspond to $F_{\rm X} \lesssim 5 \times 10^{12}\,{\rm erg\,s^{-1}\,cm^{-2}}$ ($L_{\rm X} \lesssim 3 \times 10^{33}\,{\rm erg\,s^{-1}} \approx 10^{-5.6}\,L_{\rm Edd}$). All uncertainties are quoted at the 68% (1σ) level, unless stated otherwise. We generally report X-ray fluxes and luminosities from 0.5–10 keV, except for when we discuss radio/X-ray correlations when we adopt 1–10 keV luminosities to ease comparisons with the literature (e.g., Corbel et al. 2013; Gallo et al. 2014).

2. OBSERVATIONS

We triggered joint *Chandra*/VLA observations through a cycle 16 *Chandra* target of opportunity (ToO) program (proposal ID 16400196; PI Plotkin). This program included six *Chandra* observations taken with an approximately four day cadence over a three-week period between 2015 July 15 and August 5. Exposure times generally increased over time, ranging from 4 to 43 ks. We also arranged for ToO observations with the X-ray Telescope (XRT; Burrows et al. 2005) on board the *Swift* satellite (Gehrels et al. 2004) to coincide with each *Chandra* epoch (PI Plotkin). The XRT exposures ranged from 7 to 12 ks, composed of individual 1–2 ks snapshots spread over 8–19 hr on each date, with at least one snapshot on each date simultaneous with a portion of each *Chandra* observation. On July 23, we also arranged for a simultaneous 40 ks observation with the *Nuclear Spectroscopic Telescope Array* (*NuSTAR*; Harrison et al. 2013).

Simultaneous VLA radio observations were scheduled for the beginning of each *Chandra* observation (VLA exposures also generally increased over time, but with each VLA observation being shorter than the corresponding *Chandra* one). The VLA did not obtain usable data on our second epoch (July 20). To make up for that epoch, the VLA scheduled an

Table 1
Summary of *Chandra*, *Swift*, and VLA Observations

		Chandra					*Swift*	VLA	
MJD	Date (2015)	Start Time (UT HH:MM:SS)	t_{exp} (ks)	ObsID	Gratings	Subarray	t_{exp} (ks)	Start Time (UT HH:MM:SS)	t_{exp} (ks)
(1)	(2)	(3)	(4)	(5)	(6)	(7)	(8)	(9)	(10)
57214	Jul 11	13:02:49	39.3	17701	HETG	None	1.2	…	…
57218	Jul 15	03:22:13	3.7	16702	HETG	1/2	7.3	04:12:40	0.5
57223	Jul 20	04:01:48	8.8	16703	HETG	None	10.9	…	…
57226[a]	Jul 23	08:36:58	19.3	16704	HETG	None	8.2	11:29:56	0.5
57231	Jul 28	09:42:05	17.9	16705	None	1/8	12.0	09:55:28	2.2
57233	Jul 30	…	…	…	…	…	…	09:47:36	2.2
57235	Aug 1	12:25:25	26.2	16706	None	1/8	11.7	11:24:28	5.3
57239	Aug 5	03:33:27	42.7	16707	None	1/8	9.7	03:33:00	5.6

Notes. Column (1) modified Julian date of each observing epoch. Column (2) UT date of each epoch. Columns (3)–(7) pertain to the *Chandra* observations, including the UT start times (column 3), the exposure time (column 4), the observation identification number (column 5), whether or not the HETG was in place to act as a pileup mitigation filter (column 6), and the subarray read from the ACIS chip (column 7). The *Chandra* observation from July 11 was from a separate DDT (see Section 2.6). Column (8) lists the total exposure times of the *Swift* observations, which were scheduled as series of 1–2 ks snapshots over 8–19 hr on each date, with at least one snapshot overlapping with the *Chandra* observations, except for on July 11. The *Swift* observation on July 11 was from a single snapshot that started at UT 07:03 (see Section 2.6). Columns (9)–(10) pertain to the radio observations (VLA project code SG0196), including the UT start times (column 9) and the total observing times on source (column 10). A radio observation from July 11 was obtained from the VLBA over UT 07:03–07:28, simultaneous with *Swift* on that date (but not with *Chandra*; see Section 2.6).
[a] We also obtained a 40 ks *NuSTAR* observation, taken between 2015 July 23 UT 08:21 and July 24 UT 11:01.

extra observation on July 30, for which there was not any corresponding X-ray data. Thus, we obtained observations on six dates in each waveband, and a total of five epochs included periods of strictly simultaneous overlap. We also considered a set of simultaneous X-ray and radio observations taken on July 11, obtained through separate programs (see Section 2.6). A summary of our observations appears in Table 1.

2.1. Chandra Observations and Data Reduction

For all *Chandra* observations, V404 Cygni was placed at the aimpoint of the Advanced CCD Imaging Spectrometer (ACIS; Garmire et al. 2003) S3 chip, and the data were telemetered in FAINT mode. To mitigate pileup, the first three observations were taken with the High Energy Transmission Grating (HETG; Canizares et al. 2005) in place to act as a filter, for which we analyzed the zeroth order image. The final three observations were taken without the HETG, but with the chip read in 1/8 subarray mode to reduce the exposure frame time.

The *Chandra* data reduction was performed using the *Chandra* Interactive Analysis of Observations (CIAO) software v4.8 (Fruscione et al. 2006). We first reprocessed the data to apply the latest calibration files, and we restricted the analysis to the S3 chip. We used the tool `axbary` to apply barycentric corrections to all event times, good time intervals, and aspect solutions. We next searched for time periods with elevated levels of background counts by extracting a light curve over the entire chip (from 0.5 to 7 keV), after excluding V404 Cygni and other point sources identified by the tool `wavdetect`. None of our observations displayed obvious periods of background flaring. However, in Appendix B, we describe a decision to remove the final 400 s from the first *Chandra* observation (obsID 16702), for reasons related to our spectral analysis.

Finally, we extracted spectra with the tool `specextract`, including response matrix files (rmf) and auxiliary response files (arf). Although our observational setup was designed to mitigate photon pileup as much as possible, a low-level of pileup persisted. To apply a pileup model during spectral fitting (Davis 2001), we extracted spectra containing all events with energies >0.3 keV[15], and we adopted a relatively small 4 pixel radius circular extraction region centered on V404 Cygni. We applied an energy-dependent aperture correction term to the arf file to account for the small sizes of our extraction apertures. The *Chandra* X-ray properties are listed in columns (2)–(6) of Table 2.

2.2. Swift Observations

The *Swift* XRT observations were taken in photon counting mode. We analyzed the data using the `HEASOFT` software, following standard procedures. We first reprocessed each observation with the task `xrtpipeline`, during which time we also created exposure maps for each observation to correct for bad columns on the detector. We filtered the data from 0.3–10 keV, and we extracted source photons from a circular aperture with a 25 pixel radius centered at the position of V404 Cygni. We estimated the background count rate using two circular apertures (each with a radius of 25 pixels) placed near the source, but taking care to avoid regions with enhanced soft X-ray emission from light echoes that were observed from V404 Cygni at this point in the decay (Beardmore et al. 2015a; Beardmore et al. 2016; Heinz et al. 2016; Vasilopoulos & Petropoulou 2016). For each observation, we extracted a spectrum, we built an arf with the tool `xrtmkarf` (incorporating the exposure maps created earlier), and we adopted the latest rmfs from the *Swift* calibration database. To compare to *Chandra* light curves, we applied a barycentric correction to the midpoint of each *Swift* snapshot (we did not obtain enough counts to extract useful *Swift* light curves over shorter timescales). We list the X-ray properties from each XRT observation in Table 2.

[15] See http://cxc.harvard.edu/ciao4.4/why/filter_energy.html.

Table 2
X-Ray Properties

Date (2015) (1)	*Chandra* N_{tot} (cts) (2)	*Chandra* N_{bkg} (cts) (3)	*Chandra* Net Count Rate (cts s^{-1}) (4)	*Chandra* $f_{0.5-10\,keV}$ (10^{-12} cgs) (5)	*Chandra* $L_{0.5-10\,keV}$ (10^{33} cgs) (6)	*Swift* N_{tot} (cts) (7)	*Swift* N_{bkg} (cts) (8)	*Swift* Net Count Rate (cts s^{-1}) (9)	*Swift* $f_{0.5-10\,keV}$ (10^{-12} cgs) (10)	*Swift* $L_{0.5-10\,keV}$ (10^{33} cgs) (11)	σ_{sys} (10^{-12} cgs) (12)
Jul 11[a]	3608	2.2	0.092 ± 0.002	14.0 ± 0.2	9.6 ± 1.1	314	5.5	0.257 ± 0.015	19.8 ± 1.2	13.5 ± 1.8	± 5.0
Jul 15	241	0.2	0.065 ± 0.004	8.3 ± 0.6	5.7 ± 0.8	524	14.0	0.070 ± 0.003	7.6 ± 0.3	5.2 ± 0.7	± 2.6
Jul 20	600	0.2	0.068 ± 0.003	9.6 ± 0.4	6.6 ± 0.8	1020	20.5	0.092 ± 0.003	11.0 ± 0.4	7.5 ± 0.9	± 4.8
Jul 23[b]	673	0.6	0.035 ± 0.001	4.6 ± 0.2	3.1 ± 0.4	383	15.5	0.045 ± 0.002	4.5 ± 0.2	3.1 ± 0.4	± 2.2
Jul 28	3333	1.4	0.186 ± 0.003	4.7 ± 0.1	3.2 ± 0.4	531	15.5	0.043 ± 0.002	4.8 ± 0.2	3.3 ± 0.4	± 2.7
Aug 1	3802	1.5	0.145 ± 0.002	3.6 ± 0.1	2.5 ± 0.3	403	19.0	0.033 ± 0.002	3.4 ± 0.2	2.3 ± 0.3	± 1.5
Aug 5	13651	2.4	0.320 ± 0.003	8.4 ± 0.1	5.8 ± 0.7	801	14.5	0.081 ± 0.003	8.5 ± 0.3	5.8 ± 0.7	± 4.8

Notes. Column (1): observation date. Columns (2)–(6) present information from the *Chandra* observations. Column (2): total number of counts in source aperture. Column (3): number of estimated background counts in source aperture from 0.5 to 10 keV. Column (4): net count rate. Column (5): model unabsorbed flux from 0.5 to 10 keV, in units of 10^{-12} erg s^{-1} cm^{-2}. Errors represent statistical uncertainties. Column (6): model luminosity from 0.5 to 10 keV, in units of 10^{33} erg s^{-1}. Errors include the uncertainty on the distance to the source. Columns (7)–(11) repeat the previous information for the *Swift* observations. Counts in columns (7)–(9) are reported from 0.3 to 10 keV, and model fluxes and luminosities in columns (10)–(11) are from 0.5 to 10 keV. Column (12): systematic error on the X-ray flux, based on 1σ variations in flux from the combined *Chandra* and *Swift* observations on each date (see Section 3.3).
[a] The *Chandra* observation is from a DDT program. The *Swift* observation is not simultaneous with *Chandra* (see Table 1 and Section 2.6).
[b] From *NuSTAR*, we obtained average count rates from 3 to 79 keV of 0.049 ± 0.001 and 0.045 ± 0.001 s^{-1} for FPMA and FPMB, respectively.

2.3. NuSTAR Observation

We observed V404 Cygni with *NuSTAR* on one epoch, from 2015 July 23 UT 08:21 to 2015 July 24 UT 11:01 (ObsID 90102007011). *NuSTAR* has two focal plane modules, FPMA and FPMB, and the exposure times yielded during the observation were 40.2 and 39.5 ks, respectively. We reduced the data using HEASOFT v6.19, NUSTARDAS v1.6.0, and the files from the 2016 July 6 calibration database (CALDB), and we reprocessed the data to make event files using `nupipeline`. We made light curves and energy spectra using `nuproducts` and a circular source extraction region with a radius of 60″. For background subtraction, we used a circular region with a radius of 90″ on the same detector chip where the source falls. The average source count rates in the 3–79 keV band are 0.049 ± 0.001 and 0.045 ± 0.001 s^{-1} for FPMA and FPMB, respectively. The light curve shows that the source is near these count rates over the duration of the observation except for the last ∼2 ks of the observation during which the count rate rose by a factor of two to three. In this work, we focus on the energy spectrum, which we rebinned with the requirement of an S/N of 5.0 in each spectral bin.

2.4. X-Ray Spectral Analysis

The X-ray spectral analysis was performed with the Interactive Spectral Interpretation System v1.6.2 (`ISIS`; Houck & Denicola 2000). For photoelectric absorption in our fits, we used abundances from Anders & Grevesse (1989) and cross-sections from Balucinska-Church & McCammon (1992), with updated He cross-sections from Yan et al. (1998). We briefly describe our analysis here, with more details listed in the Appendix. For spectra with <1000 counts, we binned the data to an S/N > 1.5 per bin (≳2 counts); higher-count spectra were binned to S/N > 4 per bin (≳15 counts). All fitting was performed using Cash statistics (Cash 1979), with background counts included in each fit. Reported (68%) error bars correspond to changes in the Cash statistic of $\Delta C = 1.0$ for one parameter of interest.

On each of the six epochs, we fit an absorbed power-law model (`phabs*powerlaw`) to the combined *Chandra* and *Swift* observations, where we performed a joint fit by tying the column density (N_H) and photon index (Γ) to a common value, but allowing the normalizations of each data set to independently vary. For the *Chandra* data sets, we used the Davis (2001) pileup model to correct for mild effects of photon pileup (the *Swift* data did not suffer from any pileup). Within the Davis (2001) model, we fixed the `psfrac` parameter to 0.95 (the fraction of the incident energy that falls on the central 3×3 pixels), and we left the "grade migration parameter" α free to vary (the probability of retaining n "piled" events as a single event is $p \sim \alpha^{n-1}$). The inclusion of the *Swift* data increased the number of counts, especially at soft X-rays for the first three epochs when the *Chandra* HETG was in place, and it also assisted in constraining the pileup correction (see Appendix B for further discussion).

The best-fit spectral parameters are presented in Figure 10 in the Appendix, along with a sample spectral fit to our *Chandra* observation from August 5 (our highest S/N spectrum) in Figure 11. The best-fit N_H values on each epoch were consistent with each other within the errors. Therefore, we performed another joint fit, where we forced a common N_H across all six epochs (but we allowed Γ to vary on each epoch). We found a best-fit $N_H = 8.4 \pm 0.2 \times 10^{21}$ cm^{-2}, and the best-fit photon indices are presented in Table 3, which are the values adopted throughout the rest of the text (except on July 23; see the next paragraph). The level of pileup in the *Chandra* observations from July 15 to August 5 was mild, from 2% to 5%.

On July 23, we also obtained a simultaneous observation with *NuSTAR*. To improve the spectral model, we fit the *Chandra*, *Swift*, and *NuSTAR* data from July 23 (including both the *NuSTAR* FPMA and FPMB spectra), freezing the column density to 8.4×10^{21} cm^{-2}, and forcing a common Γ. The best-fit photon index $\Gamma = 2.04 \pm 0.04$ was consistent with the best-fit value when only considering the *Chandra* and *Swift* data ($\Gamma = 1.97^{+0.08}_{-0.05}$), thereby indicating that our spectral results

Table 3
X-Ray Spectral Properties

Date (2015)	Γ	α	$f_{\rm pile}$
(1)	(2)	(3)	(4)
Jul 11[a]	1.64 ± 0.04	0.42 ± 0.07	0.08
Jul 15	1.75 ± 0.07	$0.21^{+0.69}_{-0.21}$	0.01
Jul 20	1.71 ± 0.06	0.39 ± 0.18	0.05
Jul 23	$1.97^{+0.08}_{-0.05}$	0.60 ± 0.37	0.03
Jul 23[b]	2.04 ± 0.04	…	…
Jul 28	$2.01^{+0.06}_{-0.02}$	$0.72^{+0.28}_{-0.41}$	0.03
Aug 1	$2.13^{+0.05}_{-0.01}$	$0.87^{+0.13}_{-0.65}$	0.02
Aug 5	1.99 ± 0.04	0.73 ± 0.14	0.05

Notes. Column (1) observation date. Column (2) best-fit photon index Γ. Unless marked otherwise, the spectral fits are from joint spectral fits to all *Chandra* and *Swift* data from July 15 to August 5, forcing a common best-fit column density across all epochs, while allowing Γ to vary on each date. The best-fit $N_{\rm H} = 8.4 \pm 0.2 \times 10^{21}\,{\rm cm}^{-2}$. Column (3) grade migration parameter from the Davis (2001) pileup model applied to the *Chandra* data sets. Column (4) pileup fraction in the *Chandra* data sets, as calculated by the pileup model. All X-ray spectral fits use an absorbed power-law model `phabs * powerlaw`, with abundances from Anders & Grevesse (1989) and cross-sections from Balucinska-Church & McCammon (1992), with updated He cross-sections from Yan et al. (1998).

[a] Spectral parameters from a fit to the *Chandra* data, freezing the column density to $N_{\rm H} = 8.4 \times 10^{21}\,{\rm cm}^{-2}$.

[b] Spectral parameters from a joint fit to *NuSTAR*, *Chandra*, and *Swift* data from July 23, freezing the column density to $N_{\rm H} = 8.4 \times 10^{21}\,{\rm cm}^{-2}$.

can be extended toward higher energies. Throughout the remainder of the text, we adopt $\Gamma = 2.04 \pm 0.04$ on July 23.

2.5. VLA Radio Observations

A total of six VLA observations (project code SG0196) were taken between 2015 July 15 and August 5, with on-source exposure times ranging from 8 to 93 minutes (see Table 1). Each VLA observation was scheduled to obtain as much strictly simultaneous coverage with *Chandra* as possible. As noted earlier, we did not obtain VLA observations on our second *Chandra* epoch (July 20), but we did obtain an extra VLA observation on July 30 (for which there was no corresponding X-ray observation).

The VLA was in its most extended A configuration, with a maximum baseline of 30 km. We made use of the VLA "subarray" mode, where approximately half of the VLA antennas observed at 4–8 GHz, and the other half at 8–12 GHz. We separated the two 1024 MHz basebands within each observing band to provide the broadest possible spectral coverage, while avoiding known radio frequency interference. Each 1024 MHz baseband comprised eight spectral windows, each made up of 64 2 MHz channels. The central frequencies of the basebands were 5.2, 7.5, 8.6, and 11.0 GHz. The subarrays provided a valuable frequency lever arm for investigating the radio spectrum.

The radio analysis was performed using standard procedures within the Common Astronomy Software Application v4.5 (`CASA`; McMullin et al. 2007). We calibrated each 1024 MHz baseband separately, using the Perley & Butler (2013) coefficients within the `setjy` task to set the amplitude scale. We selected our amplitude calibrator according to the local sidereal time of each observation, using 3C 286 on July 15 and August 5, and 3C 48 on all other epochs. At all epochs, we solved for the complex gain solutions toward V404 Cygni by using the secondary calibrator source J2025+3343. On July 28, we did not obtain any usable scans of a primary flux calibrator. So, we manually set the amplitude scale in `setjy` to the flux density of J2025+3343, which was determined by interpolating the flux density of J2025+3343 from the two surrounding epochs (July 23 and 30) to July 28 (the flux densities on July 23 and 30 were calculated by the task `fluxscale` when bootstrapping the amplitude gain solutions to J2025+3343 on those epochs). Over our three-week campaign, we measured flux density variations for our phase calibrator J2025+3343 at the 3, 2, 1, and 1% levels (1σ) at 5.2, 7.5, 8.6, and 11.0 GHz, respectively. We included corresponding systematic uncertainties on flux densities from July 28.

We next imaged the field surrounding V404 Cygni with the task `clean`, using Briggs weighting with a robust value of one, and two Taylor terms to model the frequency dependence of sources in the field. We placed outlier fields on two bright sources within the primary beam, so that their sidelobes did not influence the final V404 Cygni image. We achieved $1\sigma_{\rm rms}$ sensitivities from $\approx$0.010–0.035 mJy bm^{-1}, depending on the exposure time and frequency. These sensitivities are consistent with the theoretical noise limit of the VLA (for 13 antennas per frequency). Finally, we measured the flux density of V404 Cygni at each epoch by fitting a point source in the image plane using the task `IMFIT` (see Table 4).

2.5.1. Radio Spectral Indices and 8.4 GHz Flux Densities

For each radio epoch, we measured the radio spectral index $\alpha_{\rm r}$ ($f_\nu \propto \nu^{\alpha_{\rm r}}$) by fitting a power law to the four flux density measurements (via a weighted least squares fit). We estimated the uncertainty on the spectral index, $\sigma_{\alpha_{\rm r}}$, through Monte Carlo simulations. We added simulated statistical noise to each flux density (based on a Gaussian distribution with a standard deviation set to the uncertainty on each flux density measurement), and we also randomly adjusted the central frequency of each flux density across each 1024 MHz baseband (assuming a uniform distribution in frequency). We then fit a power law to each data set with random noise added, and we repeated 1000 times for each epoch. As expected, the distribution of 1000 $\alpha_{\rm r}$ measures on each epoch followed an approximately Gaussian distribution centered around zero. For $\sigma_{\alpha_{\rm r}}$, we adopted the standard deviation on 1000 simulated $\alpha_{\rm r}$ measures (which we confirmed is comparable to the 68% confidence interval). We used the above spectral fits to calculate radio flux densities (and errors) at 8.4 GHz, which are the values we generally adopt throughout this paper when displaying radio fluxes and luminosities in figures, in order to ease comparisons to the literature.

2.6. Other Multiwavelength Observations on July 11

We also considered a 39 ks *Chandra* observation granted through Director's Discretionary Time (DDT) that was taken on 2015 July 11 (obsID 17701; PIs Neilsen and Altamirano), four days before our first ToO observation. This DDT observation used the HETG, and it was obtained primarily to study a disk wind through high-resolution spectroscopy. Here, we considered only the zeroth order grating image, in order to extend our time coverage during the decay into quiescence. Analysis of this observation was performed identically to our

Table 4
Radio Properties

Date	$f_{5.2}$ (mJy bm^{-1})	$f_{7.5}$ (mJy bm^{-1})	$f_{8.6}$ (mJy bm^{-1})	$f_{11.0}$ (mJy bm^{-1})	$f_{8.4}$ (mJy bm^{-1})	$\sigma_{\rm sys}$ (mJy bm^{-1})	$(\nu L_\nu)_{8.4}$ (10^{28} erg s^{-1})	$\alpha_{\rm r}$
(1)	(2)	(3)	(4)	(5)	(6)	(7)	(8)	(9)
Jul 11[a]	0.91 ± 0.06	...	...	...	...	...	5.2 ± 0.7	...
Jul 15	0.759 ± 0.036	0.746 ± 0.032	0.827 ± 0.030	0.782 ± 0.032	0.794 ± 0.016	± 0.046	4.6 ± 0.5	0.07 ± 0.08
Jul 23	0.757 ± 0.033	0.653 ± 0.029	0.713 ± 0.029	0.703 ± 0.029	0.706 ± 0.015	± 0.053	4.1 ± 0.5	-0.09 ± 0.08
Jul 28	0.583 ± 0.024	0.570 ± 0.017	0.586 ± 0.015	0.573 ± 0.016	0.579 ± 0.009	± 0.057	3.3 ± 0.4	-0.02 ± 0.07
Jul 30	0.538 ± 0.018	0.573 ± 0.020	0.578 ± 0.022	0.643 ± 0.026	0.591 ± 0.012	± 0.051	3.4 ± 0.4	0.22 ± 0.07
Aug 1	0.372 ± 0.013	0.335 ± 0.011	0.367 ± 0.011	0.387 ± 0.012	0.369 ± 0.005	± 0.057	2.1 ± 0.2	0.07 ± 0.05
Aug 5	0.742 ± 0.011	0.801 ± 0.010	0.802 ± 0.010	0.850 ± 0.010	0.808 ± 0.005	± 0.182	4.6 ± 0.5	0.18 ± 0.03

Note. Column (1): observation date. Column (2): peak flux density in the baseband centered at 5.2 GHz. Column (3): peak flux density at 7.5 GHz. Column (4): peak flux density at 8.6 GHz. Column (5): peak flux density at 11.0 GHz. Column (6): inferred flux density at 8.4 GHz from spectral fits (see Section 2.5.1). Error bars in columns (2)–(6) represent statistical uncertainties. Column (7): systematic error on the 8.4 GHz radio flux density, based on 1σ flux density variations within each observation (see Section 3.2). Column (8): radio luminosity at 8.4 GHz. Errors include the statistical uncertainty, and the uncertainty on the distance to the source. Column (9): best-fit spectral index ($f_\nu \propto \nu^{\alpha_{\rm r}}$) for the flux densities in columns (2)–(5).
[a] VLBA observation at 5.0 GHz (see Section 2.6). We assume a flat spectral index for estimating the luminosity at 8.4 GHz.

six ToO observations. We performed two spectral fits (of the form `phabs*powerlaw`), where we first allowed $N_{\rm H}$ to vary as a free parameter (yielding $N_{\rm H} = 1.0 \pm 0.1 \times 10^{22}$ cm^{-2}, $\Gamma = 1.79 \pm 0.10$; see Figure 10), and then we fixed $N_{\rm H}$ to 8.4×10^{21} cm^{-2} (i.e., the best-fit value from Section 2.4). The latter fit yielded $\Gamma = 1.64 \pm 0.04$, which is the value we adopt throughout the text (see Table 3). We applied the Davis (2001) pileup model during these fits, and we found 8% pileup.

No VLA observations were taken on July 11. However, there was a Very Long Baseline Array (VLBA) radio program (PI Miller-Jones; project code BM421), from which we extracted radio information on July 11. Although no VLBA observations were taken simultaneously with *Chandra*, a 25 minute portion of a VLBA observation from UT 07:03–07:28 ($f_\nu = 0.91 \pm 0.06$ mJy at 5GHz) was obtained simultaneously with a *Swift* snapshot ($f_{0.5-10\,{\rm keV}} = 1.98 \pm 0.12 \times 10^{-11}$ erg s^{-1} cm^{-2}; model flux calculated in `ISIS` assuming $N_{\rm H} = 8.4 \times 10^{21}$ cm^{-2} and $\Gamma = 1.64$). For placing these data on radio/X-ray luminosity correlations, we adopted $L_{\rm R} = (5.2 \pm 0.7) \times 10^{28}$ erg s^{-1} at 8.4 GHz (assuming a flat radio spectrum) and $L_{1-10\,{\rm keV}} = (1.16 \pm 0.15) \times 10^{34}$ erg s^{-1}. Details on the VLBA reduction will be provided in an upcoming publication (J. C. A. Miller-Jones et al. 2016, in preparation).

3. RESULTS

3.1. Long-term Flux and Spectral Evolution

In Figure 1, we show the X-ray and radio light curves during our three-week campaign, along with the corresponding evolution of the X-ray photon index Γ and the radio spectral index $\alpha_{\rm r}$. Throughout our campaign, the average *Chandra* X-ray fluxes (0.5–10 keV) are a factor of 3–12 brighter than the average pre-outburst X-ray flux of V404 Cygni. Although there is an overall trend of decreasing flux with time, there is also superposed variability, so that the decay is not monotonic. Figure 1(b) displays a clear X-ray spectral softening, where the spectrum is relatively hard toward the beginning ($\Gamma = 1.64 \pm 0.04$ on July 11) and settles near the pre-outburst value of $\Gamma \approx 2$ by the end of our campaign.[16] Even though V404 Cygni re-brightens on our final epoch (August 5) to a flux comparable to July 15 ($\approx 8 \times 10^{-12}$ erg s^{-1} cm^{-2}), its X-ray spectrum remains soft on August 5 ($\Gamma = 1.99 \pm 0.04$) compared to on July 15 ($\Gamma = 1.75 \pm 0.07$).

The radio spectrum is consistent with being flat/inverted throughout our entire campaign, and only on July 30 and August 5 does it appear to be inverted at a meaningful level ($>3\sigma$) (Figure 1(d)). Throughout, we adopt 0.2 mJy (1.1×10^{28} erg s^{-1} at 8.4 GHz; Corbel et al. 2008) as the pre-outburst radio flux density, so that the radio emission is a factor of $\approx$2–5 brighter during our campaign compared to pre-outburst. However, we note that both Miller-Jones et al. (2008) and Rana et al. (2016) observe slightly higher average radio flux densities of 0.3 mJy in quiescence, implying that V404 Cygni may have temporarily reached its pre-outburst radio flux level during our campaign on August 1.

3.2. Intraday Variability

For each epoch, we create X-ray and radio light curves to explore variability on timescales of minutes to hours. X-ray light curves over three-minute time bins are displayed in Figure 2 for all seven *Chandra* observations, with fluxes from *Swift* snapshots overplotted. Five of the *Chandra* observations contain time periods with strictly simultaneous VLA coverage (ranging from 8 to 93 minutes), which we highlight as gray regions in Figure 2. For each light curve, we quantify the level of variability with the fractional rms variability amplitude statistic $F_{\rm var}$ (see, e.g., Vaughan et al. 2003), which we report in Table 5, incorporating all *Chandra* and *Swift* observations. The $F_{\rm var}$ statistic probes timescales as short as three minutes from each *Chandra* observation, and timescales as long as 8–19 hr (depending on the date), which corresponds to the range of times between the first and final *Swift* snapshots on each epoch (see Table 1). All seven X-ray light curves display variability at the $F_{\rm var} \approx 20\%$–55% level. Throughout, we (somewhat arbitrarily) require $F_{\rm var}/\sigma_{F_{\rm var}} > 1$ to claim variability, and we refer to observations displaying $1 \leqslant F_{\rm var}/\sigma_{F_{\rm var}} < 3$ as mildly variable, where $\sigma_{F_{\rm var}}$ is the statistical uncertainty on $F_{\rm var}$. Photon pileup in our *Chandra* observations could suppress the observed X-ray variability so that our $F_{\rm var}$ values are underestimated by up to a factor of 0.84 during the most extreme flares (e.g., the flare from 200 to 400 minute into the August 5 observation; see Appendix B). However, during the bulk of our observations, effects from pileup

[16] Note that we would still observe an X-ray spectral softening if we were to adopt $\Gamma = 1.79 \pm 0.10$ on July 11 when allowing the column density to vary as a free parameter.

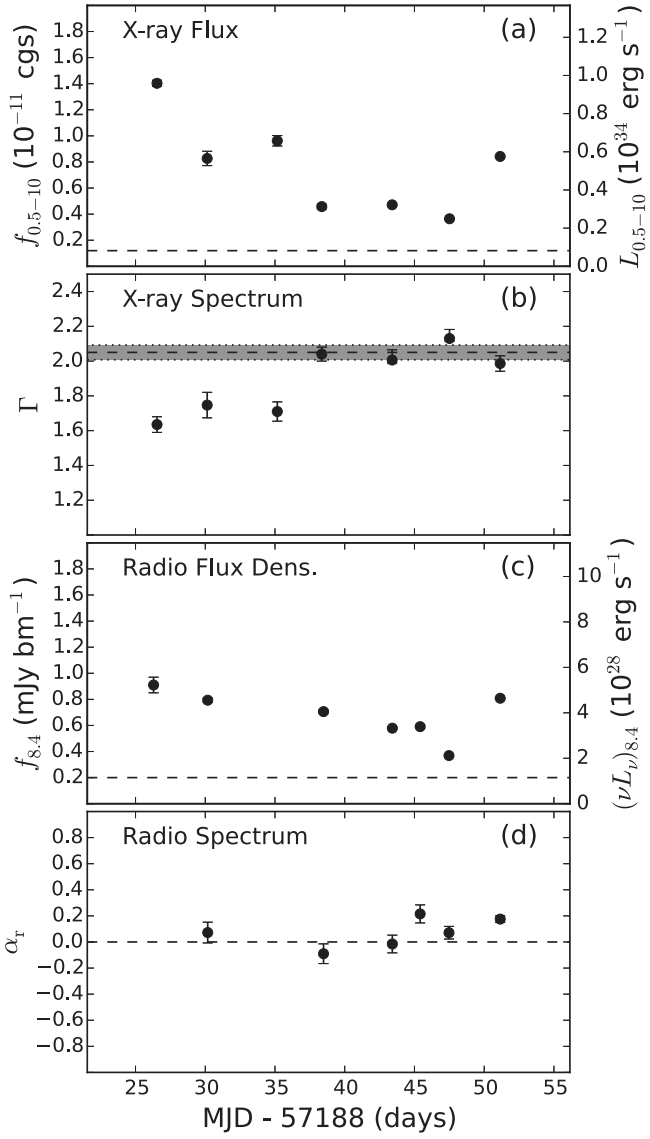

Figure 1. (a) *Chandra* X-ray light curve during our three-week campaign. Unabsorbed X-ray fluxes (luminosities) from 0.5 to 10 keV are labeled on the left (right) vertical axis. The dashed line illustrates the average pre-outburst X-ray flux (Bernardini & Cackett 2014). (b) Evolution of the X-ray photon index. The dashed line and gray shaded region denote the pre-outburst Γ and 1σ uncertainty from Reynolds et al. (2014). (c) Interpolated radio flux density light curve at 8.4 GHz (see left vertical axis); corresponding luminosities at 8.4 GHz are labeled on the right vertical axis, and the dashed line shows the pre-outburst radio flux density (Corbel et al. 2008). (d) Radio spectral index α_r (we do not have radio spectral constraints from the July 11 VLBA observation). The dashed line marks a flat radio spectrum for reference. In all panels, the time axis is referenced to the discovery date of the outburst (2015 June 15).

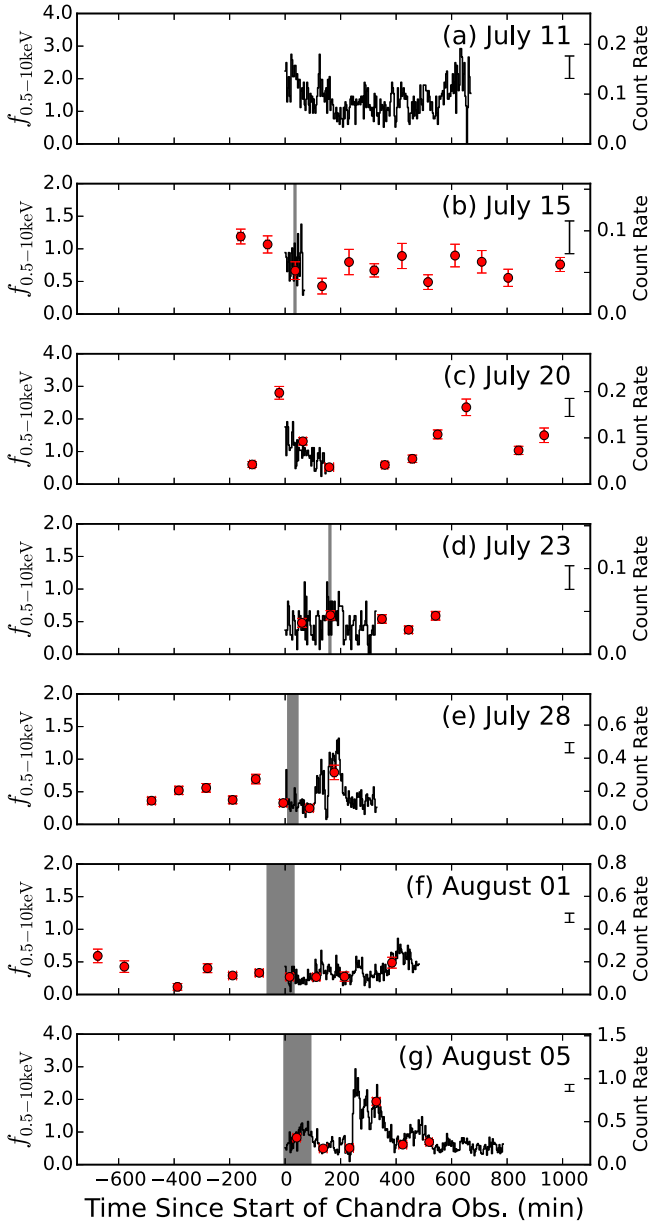

Figure 2. X-ray light curves of seven *Chandra* observations binned by three minutes (black solid lines), with typical error bars illustrated in the top right of each panel. X-ray fluxes from ≈1–2 ks *Swift* snapshots are overplotted (red circles). Shaded regions mark when the VLA observed. X-ray fluxes are from 0.5 to 10 keV, in units of 10^{-11} erg s^{-1} cm^{-2} (see left vertical axes), and count rates for the *Chandra* observations are listed on the right vertical axes. The *x*-axis is referenced to the start time of each *Chandra* observation (see Table 1; times from all telescopes are barycentered).

are generally more mild. We do not obtain a sufficient number of counts in each three-minute bin to investigate short-term spectral variability in the X-ray; though, we note in Appendix B that we do not see evidence for X-ray spectral variability within individual *Chandra* exposures binned by count rate. For completeness, we search for quasiperiodic oscillations in our highest count rate *Chandra* observation (August 5), and we see no evidence from 0.001 to 1 Hz.

For our six VLA epochs, we split each radio observation into three-minute time bins, which we image at each central frequency (following the same procedure described in Section 2.5). We have sufficient radio signal to also investigate radio spectral variability. For each time bin, we fit a power law to the radio spectrum to measure α_r and infer the radio flux density at 8.4 GHz, following the procedure in Section 2.5.1. For each time bin, we typically measure flux densities to accuracies of $\sigma_f \approx \pm 0.03$–$0.04$ mJy bm^{-1} and spectral indices to $\sigma_{\alpha_r} \approx \pm 0.1$–$0.3$. Light curves for the 8.4 GHz radio flux density and for the radio spectral index α_r are displayed in Figures 3 and 4, respectively (we omit our first two radio epochs because they contain <10 minute on source). V404 Cygni displays strong radio variability during our final August 5 epoch ($F_{\rm var} = 0.22 \pm 0.01$), and to lesser extents on August 1 ($F_{\rm var} = 0.12 \pm 0.03$) and July 28 ($F_{\rm var} = 0.09 \pm 0.04$; see

Table 5
Variability

Date (2015)	Full Exposures		Strictly Simultaneous			
	$F_{\rm var,xray}$	$F_{\rm var,radio}$	$F_{\rm var,xray}$	$F_{\rm var,radio}$	$t_{\rm exp,sim}$ (minute)	p
(1)	(2)	(3)	(4)	(5)	(6)	(7)
Jul 11	0.25 ± 0.03	...	...	...	...	...
Jul 15	0.18 ± 0.10	0.04 ± 0.19	0.11 ± 0.85	0.04 ± 0.19	8	...
Jul 20	0.39 ± 0.05	...	...	...	...	...
Jul 23	0.24 ± 0.09	0.06 ± 0.17	0.37 ± 0.07	0.06 ± 0.17	8	...
Jul 28	0.54 ± 0.05	0.09 ± 0.04	0.29 ± 0.13	0.09 ± 0.04	35	0.2
Jul 30	...	0.04 ± 0.08	...	...	...	...
Aug 01	0.36 ± 0.05	0.12 ± 0.03	0.39 ± 0.13	0.09 ± 0.07	32	0.4
Aug 05	0.55 ± 0.02	0.22 ± 0.01	0.28 ± 0.03	0.22 ± 0.01	93	0.003

Note. Column (1): observation date. Column (2): the $F_{\rm var}$ statistic (with 1σ statistical uncertainties), which quantifies the rms flux variability for the full combined *Chandra* and *Swift* X-ray light curves (July 11 is based only on *Chandra* observations). Column (3): $F_{\rm var}$ for the full duration of each VLA radio light curve. Columns (4)–(5): same as previous two columns, but over the time periods with strict simultaneity between *Chandra* and the VLA (*Swift* data omitted). Note that columns (3) and (5) only differ on August 1, which is the only time that a VLA observation began before *Chandra*. Column (6): duration of simultaneous overlap (reported as the total VLA time on source). Column (7): the probability of no correlation between the radio and X-ray fluxes, for the three epochs with the most simultaneous overlap.

Table 5). Intriguingly, we do not see rapid intraday fluctuations in $\alpha_{\rm R}$, in contrast to Rana et al. (2016) who observe the radio spectrum to fluctuate between optically thin and optically thick over 10-minute time intervals (though we note that we observed when V404 Cygni was up to a factor of three radio brighter, and a detailed comparison is out of the scope of this paper).

Finally, we consider the five epochs, where the *Chandra* and VLA observations contain periods of strict simultaneity (July 15, July 23, July 28, August 1, and August 5). For a proper comparison, we apply barycentric corrections to the times of each three-minute VLA time bin, and we extract *Chandra* light curves over strictly simultaneous three-minute bins. The $F_{\rm var}$ statistic is reported in Table 5 for each portion of these five radio and X-ray observations with strict simultaneity (we also report in Table 5 the length of strict overlap). We detect X-ray variability in $4/5$ epochs (though most significantly on August 5), and we detect radio variability only on August 5. For the final three epochs with >30 minutes of strict simultaneity (July 28, August 1, and August 5), we search for correlated X-ray and radio variations using a Pearson correlation test. There is a hint for a weak, but not highly significant, correlation on August 5 ($p = 0.003$ that no correlation is present; see Figure 5 for a comparison of the radio and X-ray light curves on August 5), which we describe further in the next subsection. There is no evidence for correlated X-ray/radio variations on either July 28 ($p = 0.2$) or August 1 ($p = 0.4$).

3.2.1. August 5: Correlated Variability and a Radio Lag?

The August 5 epoch shows strong variability in both the X-ray and radio, with a marginally significant correlation between the X-ray and radio fluxes. Examination of the X-ray and radio light curves (Figures 2, 3, and 5) suggests that V404 Cygni began a small flare at the time when both *Chandra* and the VLA were observing. We calculate the cross-correlation function (CCF) for the 1–10 keV X-ray and 8.4 GHz radio light curves[17] over the 93-minute period of overlap (using three-minute time bins that are strictly simultaneous; we adopt 1–10 keV X-ray fluxes here for consistency with our radio/X-ray luminosity correlation analysis in Section 3.3, but results are unchanged if we adopt 0.5–10 keV fluxes). Our radio and X-ray light curves lack sufficient time coverage to define a non-flaring continuum level. Therefore, when calculating the CCF, we apply the locally normalized discrete correlation function algorithm described by Lehar et al. (1992).

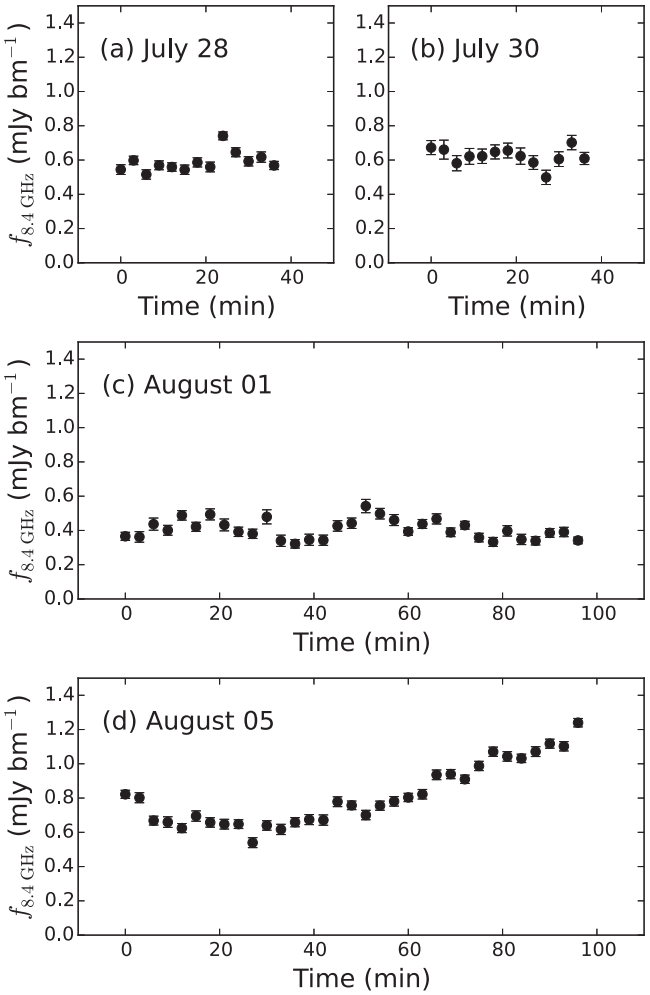

Figure 3. Radio light curves for the four epochs with the longest amount of radio coverage, binned by three minutes. The x-axis is referenced to the start time of each VLA observation.

[17] CCF results on the light curves from July 28 and August 1 are inconclusive, which is to be expected since we do not observe obvious X-ray flares during the (shorter) ≈30 minute periods of overlap on those dates.

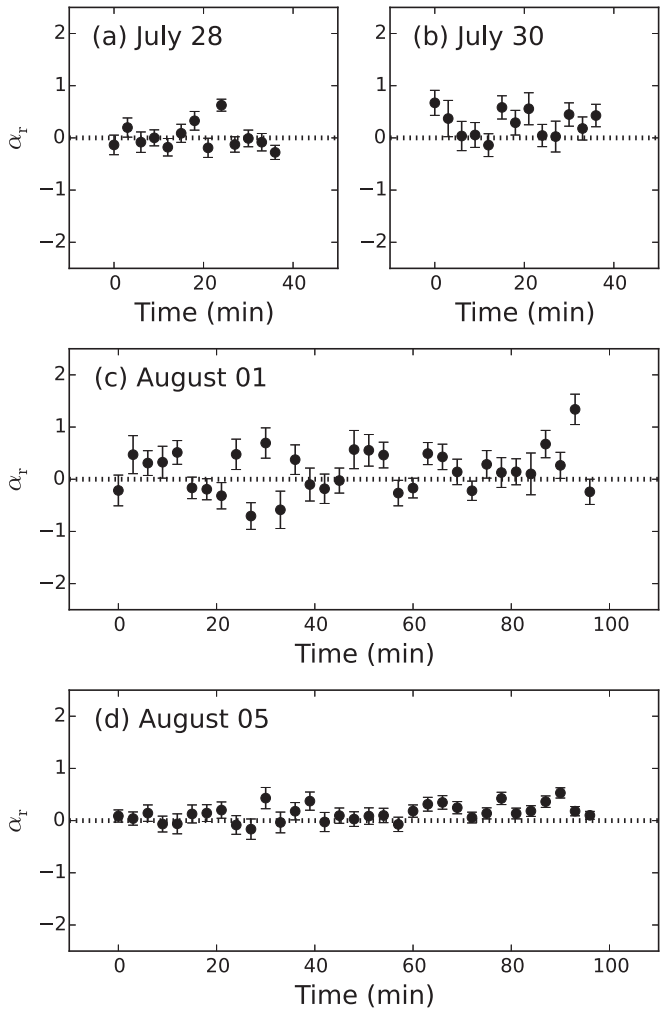

Figure 4. Variation of radio spectral index with time for the four longest radio epochs (binned by three minutes). The dotted lines mark $\alpha_r = 0$ for reference. The x-axis is referenced to the beginning of each VLA observation.

This algorithm is similar to the discrete correlation function (e.g., Edelson & Krolik 1988), except, at a given time delay, the first and second moments of each time series are calculated by considering only the subset of data pairs within each time delay bin, instead of over the entire time series.

The CCF over these 93 minutes of strict simultaneity is displayed in Figure 6. Error bars are calculated through the following bootstrapping method that simulates the expected CCF for uncorrelated variations: we randomize each radio and X-ray light curve 1000 times (after adding random statistical noise to each data point according to the flux measurement uncertainties), and we then calculate the CCF on each realization of the data. The error bars in Figure 6 display the standard deviations at each time delay for the 1000 bootstrapped CCFs. The CCF peaks (i.e., shows the strongest positive correlation) at a time delay of $\Delta t = -15.4 \pm 4.0$ minutes, where a negative time delay indicates that the radio emission lags the X-ray emission.[18] The value of the CCF at $\Delta t = -15$ minute is 0.76 ± 0.22. To estimate the statistical significance of delayed correlated variability, we use the above simulations to calculate a global significance level (following Bell et al. 2011). We determine the fraction of simulated CCF values at any time delay with a value >0.76, and we find $p = 0.01$. This global significance level accounts for stochastic fluctuations as well as false detections from any intrinsic yet uncorrelated variability within each light curve (see Bell et al. 2011 for details).

As noted earlier, the observed radio and X-ray emission are correlated at a marginally significant level ($p = 0.003$, from a Pearson correlation test). However, if we remove the radio lag by shifting the radio light curve by 15 minutes (Figure 5(d)) and then re-extract the X-ray light curves over three-minute bins, then the correlated radio and X-ray variability becomes more statistically significant ($p = 7 \times 10^{-5}$; Figure 5(e)). For completeness, we also perform a linear regression to the radio/X-ray correlations over the 93 minutes of strict simultineity, and we find a marginally steeper slope after removing the radio lag ($f_r \propto f_x^{0.42\pm0.15}$ as observed, and $f_r \propto f_x^{0.59\pm0.17}$ after removing the radio delay; see Section 3.3 for a description of our fitting method).

We stress that we consider the evidence for a radio time delay to be tentative at the moment, as the $p = 0.01$ chance of a random correlation yields only a marginal detection. Furthermore, the light curves supporting this CCF analysis are not optimal, as we did not observe the beginning of the flare in the X-ray, nor did we observe the maximum of the flare in the radio. Nevertheless, we report the CCF results here in order to highlight a result that merits further investigation, but we proceed cautiously with our interpretation (see Section 4.3).

3.3. Radio—X-Ray Luminosity Correlation

In Figure 7, we add our five new epochs of simultaneous VLA/*Chandra* observations, along with the VLBA/*Swift* observations from July 11, to the radio/X-ray luminosity correlation for V404 Cygni. We compare to quasi-simultaneous data from the 1989 outburst and to two epochs of simultaneous observations in quiescence, as described in Section 3.4. Our 2015 campaign filled in a luminosity regime that was not well covered during the 1989 outburst, and to our knowledge, no other radio telescope covered these luminosities in 2015.

The error bars displayed in Figure 7 for our 2015 campaign include statistical uncertainties from the flux measurements (with the distance uncertainty propagated, to ease comparisons to the literature), and a systematic error set to the standard deviations of the intraday flux variability on each epoch (see Tables 2 and 4). For the July 11 VLBA observation, we assume a systematic error of 0.15 dex. Errors for the data points taken from the literature are described in Section 3.4 (where we assume that flux uncertainties for the quasi-simultaneous observations are dominated by variability induced systematics). Following Gallo et al. (2014), we fit a function of the form $(\log L_R - 29) = b + m(\log L_X - 35)$ to the updated radio/X-ray luminosity correlation, using the Bayesian linear regression technique of Kelly (2007). We obtain nearly identical results as Corbel et al. (2008) and Gallo et al. (2014), who consider the 1989 and 2003 data. We find $b = 0.40 \pm 0.04$, $m = 0.54 \pm 0.03$, and $\sigma_{\rm int} = \pm 0.06 \pm 0.03$.

Since all of our 2015 X-ray observations are longer than our radio observations, we also re-image our radio and X-ray observations to only include strictly simultaneous time periods,

[18] To estimate the time delay (Δt) and error ($\sigma_{\Delta t}$), we consider data points in the CCF between $-48 < \Delta t < 18$ minutes (which corresponds to the full-width half-maximum of the peak in the CCF). We then calculate Δt and $\sigma_{\Delta t}$, respectively, as the average time and standard deviation, weighted by the CCF.

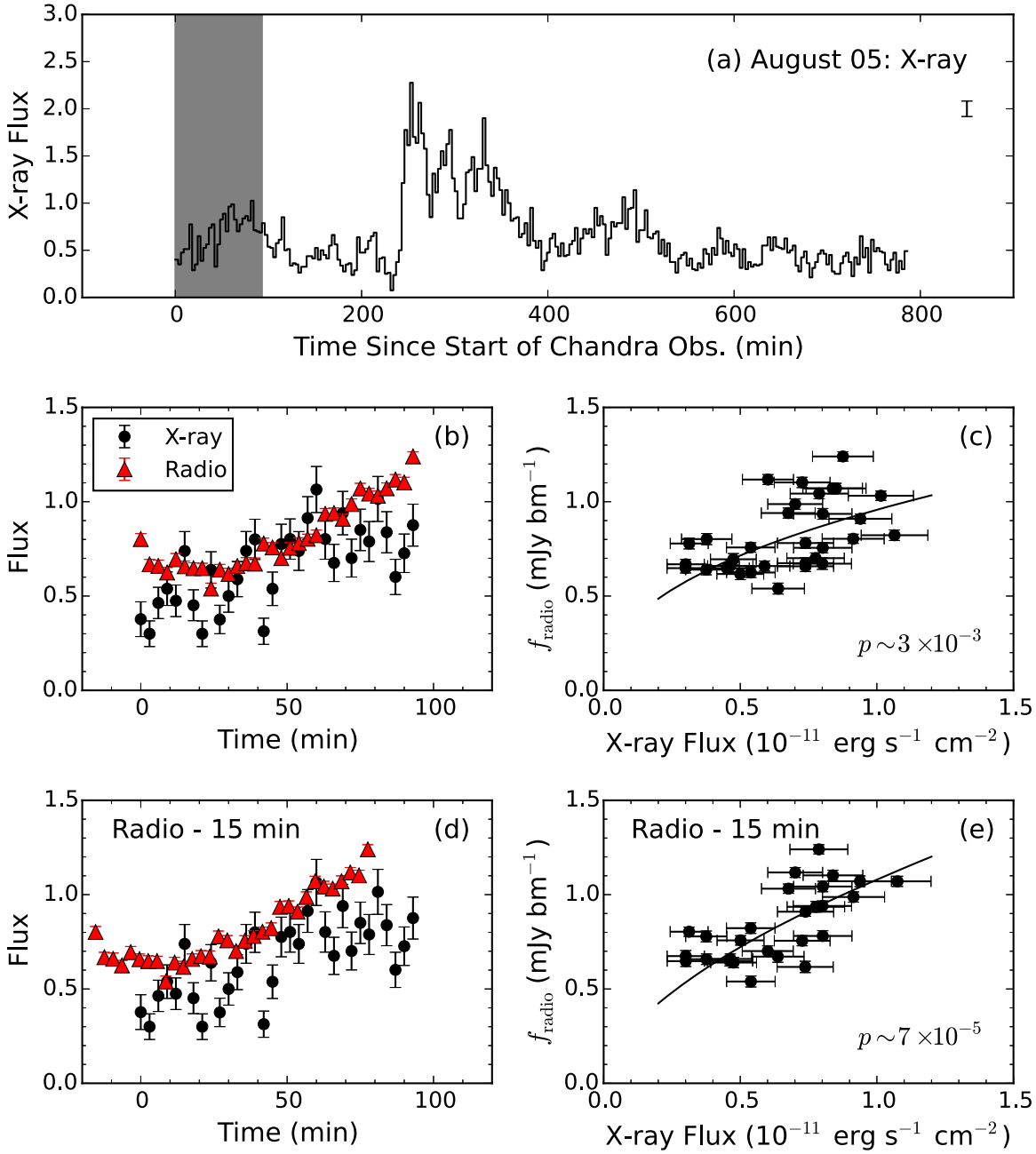

Figure 5. (a) The hard (1–10 keV) *Chandra* X-ray light curve from August 5 (binned by 3 minute), with the shaded region denoting the time period with strictly simultaneous VLA observations. A typical error bar is illustrated in the top right corner. (b) X-ray (black circles) and radio (red triangles) light curves during the period of strict simultaneity. (c) Radio vs. X-ray emission. A Pearson correlation test indicates a (marginal) positive correlation at the $p \approx 3 \times 10^{-3}$ level. The black solid shown shows the best-fit radio/X-ray correlation during the 93 minutes of strict simultaneity ($L_{\rm R} \propto L_{\rm X}^{0.4 \pm 0.2}$). (d) Same as panel (b), except with the radio data delayed by 15 minutes. (e) Same as panel (c), except with X-ray light curves re-extracted after factoring in the 15-minute radio delay. After correcting for the time delay, a Pearson correlation test indicates a stronger correlation ($p \approx 7 \times 10^{-5}$), and $L_{\rm R} \propto L_{\rm X}^{0.6 \pm 0.2}$. All X-ray fluxes are from 1 to 10 keV (in units of 10^{-11} erg s^{-1} cm^{-2}), and all radio flux densities are at 8.4 GHz (in units of mJy bm^{-1}); the normalizations of the radio and X-ray light curves in panels (b) and (d) correspond to the aforementioned units.

in order to investigate how non-simultaneity may influence the radio/X-ray correlation. We find the difference to be negligible, and well within the attributed measurement errors and scatter about the luminosity correlation: the radio luminosities are hardly affected, and no X-ray luminosity changes by more than 0.2 dex. We similarly do not find any impact to the radio/X-ray correlation if we consider periods of strict overlap after removing the 15-minute radio time delay.

3.4. Comparison Observations from the Literature

Here, we describe comparison data from other X-ray and radio campaigns on V404 Cygni in the literature. Our comparison data is comprised primarily of quasi-simultaneous radio and X-ray observations from the 1989 outburst, as compiled by Corbel et al. (2008), and two epochs of simultaneous radio and X-ray observations in quiescence (pre-2015 outburst), one from the VLA/*Chandra* in 2003

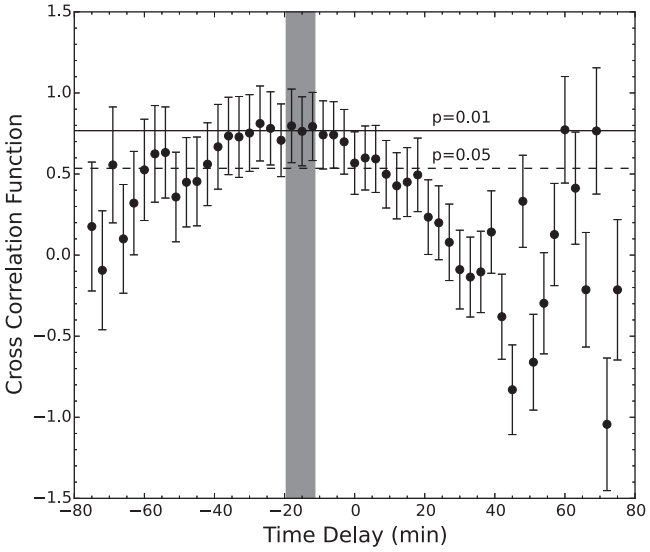

Figure 6. Cross-correlation function (CCF) for the strictly simultaneous X-ray and radio light curves on August 5. Negative time delays mean that the radio emission lags the X-ray emission. The CCF shows marginal evidence for the radio emission lagging the X-ray by 15 ± 4 minutes (the shaded region illustrates the $\pm 1\sigma$ confidence interval on the time delay). The solid and dashed horizontal lines mark the $p = 0.01$ and $p = 0.05$ probabilities, respectively, that the CCF peak is due to random fluctuations and/or uncorrelated variability (see Section 3.2.1).

(Hynes et al. 2004, 2009; Corbel et al. 2008), and one from the VLA/*NuSTAR* in 2013 (Rana et al. 2016). We also adopt X-ray spectral parameters from the literature based on three additional X-ray observations taken pre-outburst from *Chandra*, *XMM-Newton*, and *Suzaku* (Reynolds et al. 2014) and one *Chandra* observation taken after the outburst in 2015 November (Tomsick et al. 2015; see Section 3.4.3).

3.4.1. Corbel et al. (2008)

Corbel et al. (2008) assemble a total of 20 epochs of quasi-simultaneous radio and X-ray observations of V404 Cygni during the decay of its 1989 outburst, with luminosities ranging from $10^{34} < L_X < 10^{37}$ erg s^{-1}. Although the statistical measurement errors on each data point are typically $\approx$10%, we adopt larger uncertainties here, to account for the radio and X-ray data not being strictly simultaneous, and to account for the lack of detailed spectral information for each data point. Following Gallo et al. (2014), we adopt errors of 0.15 and 0.30 dex on each radio and X-ray luminosity, respectively. Corbel et al. (2008) also re-examine strictly simultaneous *Chandra* and VLA observations of V404 Cygni in quiescence from 2003 July 28–29 (56 ks with *Chandra* and 14 hr with the VLA; also see Hynes et al. 2004, 2009). We adopt their X-ray and radio flux measurements, including a 3–9 keV X-ray flux of $1.79^{+0.13}_{-0.06} \times 10^{-13}$ erg s^{-1} cm^{-2} and a radio flux density of 0.193 ± 0.022 mJy at 8.4 GHz (they find a radio spectral index of $\alpha_r = 0.29 \pm 0.46$). For placing these observations onto the radio/X-ray plane, the above fluxes correspond to X-ray and radio luminosities of $L_X = 2.8 \times 10^{32}$ erg s^{-1} (1–10 keV) and $L_R = 1.1 \times 10^{28}$ erg s^{-1} (8.4 GHz). We adopt 30% systematic uncertainties on these X-ray and radio fluxes to account for variability in each band during the strictly simultaneous observations (0.13 dex).

3.4.2. Rana et al. (2016)

Rana et al. (2016) present VLA observations in quiescence taken on 2013 December 2, along with three epochs of *NuSTAR* X-ray observations (2013 October 13, October 14, and December 2) and one epoch of *XMM-Newton* observations (2013 October 13). Here, we only consider their simultaneous radio and X-ray epochs from December 2, which includes 9 hr with the VLA and 25 ks with *NuSTAR*.

Their VLA observations are from 5 to 8 GHz, and they provide radio flux density measurements at four central frequencies (each with 512 MHz bandwidth; see their Table 3). To compare to 8.4 GHz flux densities from our 2015 campaign, we fit a power law to their published 5–8 GHz radio spectrum, using the same routine described in Section 2.5.1. We find a radio spectral index $\alpha_r = -0.27 \pm 0.05$ and $f_{8.4} = 0.274 \pm 0.082$ mJy ($L_R = 1.6 \times 10^{28}$ erg s^{-1}).

For the X-ray flux coinciding with their VLA observation, we estimate an absorbed 3–10 keV X-ray flux of 2.5×10^{-13} erg s^{-1} cm^{-2} during their December 2 *NuSTAR* epoch (see their Figure 6). Using their best-fit power-law spectrum to V404 Cygni in quiescence ($N_H = 1.2 \times 10^{22}$ cm^{-2} and $\Gamma = 2.12 \pm 0.07$; 90% confidence), we estimate $f_{1-10\,\mathrm{keV}} = 5.4 \times 10^{-13}$ erg s^{-1} cm^{-2} ($L_X = 3.7 \times 10^{32}$ erg s^{-1}). The difference in N_H obtained by Rana et al. (2016) compared to our best-fit N_H in Section 2.4 is because Rana et al. adopt Wilms et al. (2000) abundances during their fits, and we adopt Anders & Grevesse (1989) abundances (see Appendix A). We add 30% systematic errors (0.13 dex) to both the radio and X-ray luminosities to account for variability.

3.4.3. Quiescent X-Ray Spectra

Reynolds et al. (2014) take a comprehensive look at four pre-outburst X-ray spectra, obtained by *Chandra*, *XMM-Newton*, and *Suzaku*. Over these four epochs, they find 0.3–10 keV X-ray fluxes ranging from 0.8×10^{-12}–3.4×10^{-12} erg s^{-1} cm^{-2}, and Γ ranging from 1.95 to 2.25. They also perform a joint spectral fit to these four spectra, forcing a common column density and power-law component, obtaining $\Gamma = 2.05 \pm 0.07$ and $N_H = (1.15 \pm 0.07) \times 10^{22}$ cm^{-2} (90% confidence). We adopt $\Gamma = 2.05$ as the "canonical" pre-outburst X-ray spectrum. Although Reynolds et al. (2014) favor a larger column density than our study (likely because they adopt different abundances, from Asplund et al. 2009), adopting their $\Gamma = 2.05$ will not systematically influence our conclusions. Earlier studies based on the same pre-outburst *Chandra* (two epochs) and *XMM-Newton* observations (1 epoch) quote best-fit column densities similar to our study—$0.75^{+0.15}_{-0.08} \times 10^{22}$ and $0.81 \pm 0.01 \times 10^{22}$ cm^{-2} from *Chandra* (Corbel et al. 2008), and $0.88 \pm 0.6 \times 10^{22}$ cm^{-2} from *XMM-Newton* (Bradley et al. 2007). Those earlier studies find photon indices of $\Gamma = 2.1 \pm 0.3$, 2.17 ± 0.13, and 2.09 ± 0.08, respectively, which are consistent with the range of Γ in Reynolds et al. (2014).

We also include a *Chandra* observation of V404 Cygni obtained by Tomsick et al. (2015) on 2015 November 27 (obsID 17245; PI Tomsick; note that this was 26 days before V404 Cygni flared again on 2015 December 23; Beardmore et al. 2015b). This post-outburst observation shows X-ray properties similar to pre-outburst, including $N_H = (1.1 \pm 0.3) \times 10^{22}$ cm^{-2} (using Wilms et al. 2000 abundances), $\Gamma = 2.0 \pm 0.3$ (90% confidence), and an absorbed 0.3–10 keV flux of 7.6×10^{-13} erg s^{-1} cm^{-2}. When we display values from Reynolds

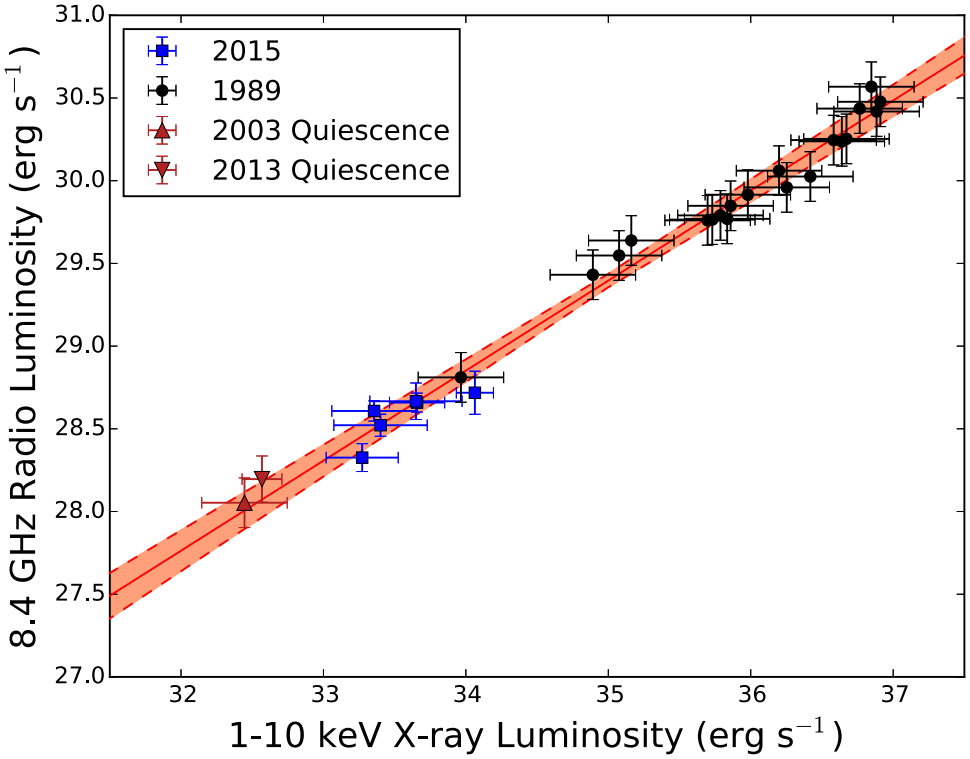

Figure 7. Radio/X-ray luminosity correlation for V404 Cygni. Blue squares show observations from our 2015 campaign, including the simultaneous VLBA and *Swift* observations on July 11. Black circles show data from the 1989 decay (Corbel et al. 2008), and the red triangles show two pre-outburst epochs: 2003 (Corbel et al. 2008; Hynes et al. 2009) and 2013 (Rana et al. 2016). The red solid line and shaded region show the best fit to the radio/X-ray correlation ($L_{\rm R} \propto L_{\rm X}^{0.54}$) and the 1σ uncertainty.

et al. (2014) and Tomsick et al. (2015) in upcoming figures, we convert their reported 0.3–10 keV fluxes to 0.5–10 keV.

4. DISCUSSION

In Figure 8, we display the X-ray spectral evolution of V404 Cygni as a function of Eddington ratio. This figure supports the statistical assertion by Plotkin et al. (2013) that the spectral softening occurs over a narrow range of luminosity, before the BHXB reaches its minimum (i.e., pre-outburst) quiescent luminosity. From Figure 1, V404 Cygni reaches $\Gamma \approx 2$ between July 23 and August 1, which indicates that V404 Cygni re-enters the quiescent spectral state around $L_{0.5-10\,{\rm keV}} = 2.5$–$3.2 \times 10^{33}$ erg s^{-1} ($-5.6 \lesssim \log L_X/L_{\rm Edd} \lesssim -5.5$), and that the transition into quiescence occurs over only a factor of $\approx$3 in luminosity. This luminosity where V404 Cygni enters quiescence is lower than the $10^{-5}\,L_{\rm Edd}$ threshold suggested by Plotkin et al. (2013), but it is still a factor of $\approx$3–4 above the average pre-outburst quiescent luminosity of 8×10^{32} erg s^{-1} for V404 Cygni (0.5–10 keV; Bernardini & Cackett 2014). Sivakoff et al. (2015b) suggest that V404 Cygni did not settle back to its pre-outburst $L_{\rm X}$ until sometime between August 5 and 21 (interestingly, the optical emitting outer disk did not return to its pre-outburst flux level until 2015 October 10–20; Bernardini et al. 2016b).

The X-ray variability properties of V404 Cygni during our campaign are also comparable to pre-outburst, as our maximum measured X-ray $F_{\rm var} = 55 \pm 2\%$ is similar to $F_{\rm var} = 57.0 \pm 3.2\%$ reported by Bernardini & Cackett (2014). We also demonstrate that the X-ray spectral softening is not accompanied by corresponding changes in the shape of the radio spectrum from the outer jet (Han & Hjellming 1992 also observed flat/inverted radio spectra at comparable radio flux densities during the decay of the 1989 outburst). The normalization of the radio/X-ray luminosity correlation appears identical between the 2015 and 1989 outbursts, thereby suggesting a robust disk/jet coupling for V404 Cygni. The BHXB GX 339−4 also displays nearly identical correlation slopes and normalizations between different outbursts (Corbel et al. 2013).

4.1. Comments on RIAF X-Ray Emission

Our data are consistent with an RIAF origin for the X-rays from V404 Cygni, as long as the X-ray emission is very inefficient throughout the entire decay as described below.[19] We can parameterize the X-ray luminosity as $L_{\rm X} \propto \dot{M}^q$, where q describes the radiative efficiency (for convenience, we will refer to q as the "radiative efficiency") and $\dot{M}$ is the mass accretion rate through the inner regions of the accretion flow. For a partially self-absorbed synchrotron jet, the radio luminosity follows $L_{\rm R} \propto Q_{\rm j}^{17/12-(2/3)\alpha_{\rm r}}$, where the jet power, $Q_{\rm j}$, is linearly proportional to $\dot{M}$ (e.g., Falcke & Biermann 1995). We adopt $\alpha_{\rm r} = 0$, such that the slope of the radio/X-ray correlation $m = (17/12)/q$. For V404 Cygni, $m \approx 0.5$, which implies an X-ray efficiency of $q \approx 2.8$ (for the most inverted radio spectrum observed during our campaign, $\alpha_{\rm r} \approx 0.2$, the implied X-ray efficiency is $q \approx 2.6$, and an inverted radio spectrum does not alter our conclusions). This

[19] We note, however, that there are arguments against an RIAF interpretation for V404 Cygni in the literature, including a lack of X-ray emission lines from V404 Cygni in quiescence (e.g., Bradley et al. 2007; Rana et al. 2016), and also UV emission that is inconsistent with most RIAF models unless an outflow is incorporated (Hynes et al. 2009).

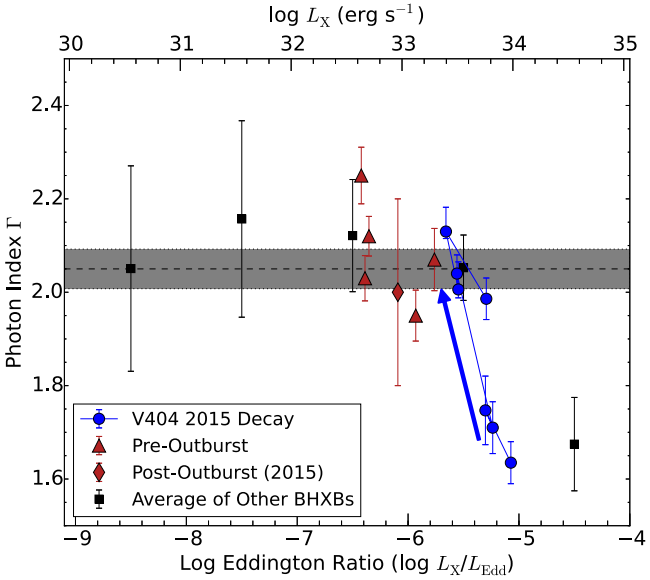

Figure 8. X-ray spectral evolution of V404 Cygni as a function of Eddington ratio (L_X/L_{Edd}, where L_X, which is displayed along the top axis, is calculated from 0.5 to 10 keV). Blue circles represent observations from our 2015 decay, with the blue solid lines connecting the data points to illustrate the evolution with time (following the direction of the blue arrow). Red triangles show spectral fits from pre-outburst observations compiled from Reynolds et al. (2014) and Rana et al. (2016), the red diamond represents a *Chandra* observation from 2015 November (Tomsick et al. 2015), and black squares represent the average photon indices of 10 quiescent BHXBs binned by Eddington ratio, from Plotkin et al. (2013). The X-ray spectral softening occurs over a narrow range in Eddington ratio (from $10^{-5.1}$ to $10^{-5.6}$), which is more luminous than the average pre-outburst Eddington ratio ($10^{-6.2}$; Bernardini & Cackett 2014). The dashed line and gray shaded region illustrate the average Γ and 1σ confidence interval for V404 Cygni pre-outburst (from Reynolds et al. 2014).

efficiency is consistent with expectations from many RIAF models. For example, Merloni et al. (2003) calculate that the X-ray efficiency may range from $q_{RIAF} \approx 2.0$–3.4 at the lowest accretion rates.

It is beyond the scope of this paper to explore specific RIAF models in detail. However, any model must satisfy other observational constraints besides $q \approx 2.8$. One is the relatively rapid X-ray spectral softening. In a hot accretion flow, synchrotron self-Compton (SSC) processes are important for generating X-ray emission (see, e.g., recent reviews by Poutanen & Veledina 2014; Malzac 2016), and the X-ray spectral softening toward quiescence is generally expected to be driven by a lower optical depth to inverse Compton scatterings and/or a lower flux of seed photons as $\dot{M}$ decreases (e.g., Esin et al. 1997; Tomsick et al. 2001; Sobolewska et al. 2011; Niedźwiecki et al. 2014). However, for V404 Cygni, our monitoring campaign demonstrates that such a decrease in optical depth/seed photon flux cannot be accompanied by a large change in the the X-ray efficiency q, since the slope of the radio/X-ray correlation does not change at a detectable level (i.e., the uncertainty on the best-fit $m = 0.54 \pm 0.03$ implies $\sigma_q \approx \pm 0.08$). Furthermore, the X-ray variability properties of V404 Cygni are similar across our entire campaign and pre-outburst, in both flux amplitude and timescale, which may indicate that the size of the X-ray emitting region does not evolve significantly.

4.2. Comments on Jet Synchrotron X-Ray Emission

Several studies of V404 Cygni in quiescence have favored a synchrotron origin for the X-ray emission (e.g., Bernardini & Cackett 2014; Xie et al. 2014; Markoff et al. 2015). In this case, the observed $\Gamma \approx 2$ implies that the synchrotron emitting particles are radiatively cooled (see, e.g., Plotkin et al. 2013), and/or that the particle acceleration mechanisms along the jet become less efficient as luminosity decreases (i.e., the maximum Lorentz factor of accelerated particles becomes smaller, see, e.g., Connors et al. 2016 for recent discussions on both scenarios).

In the case of radiatively cooled particles, the X-ray spectral softening implies a switch in the X-rays from being dominated by the RIAF and/or by the optically thin jet in the hard state, to becoming dominated by a (synchrotron-cooled) jet in quiescence (Yuan & Cui 2005). However, as described below, our 2015 campaign excludes a synchrotron-cooled jet in quiescence, unless the emission is scattered into the X-ray waveband through SSC. For synchrotron-cooled X-rays, the radiative efficiency $q_{cool} = p + 2 - (3/2)\Gamma$ (Heinz 2004), where p describes the energy distribution of the synchrotron emitting particles before they are cooled by radiative losses (i.e., below the cooling break, the number density of relativistic particles $n_e \propto \gamma^{-p}$, where γ is the Lorentz factor of the emitting particles). For $2.0 < p < 2.3$ (which is typical in astrophysical contexts; e.g., Bell 1978; Drury 1983; Achterberg et al. 2001), $\Gamma = 2$ yields $1.0 < q_{cool} < 1.3$, which results in a steeper radio/X-ray correlation slope of $1.1 < m_{cool} < 1.4$ (for an inverted $\alpha_r \approx 0.2$, the shallowest slope supported by our data would be $m_{cool} \approx 1.0$).

If X-rays are to become synchrotron cooled in quiescence, then the transition must occur at $L_X \approx 3 \times 10^{33}$ erg s^{-1} (i.e., where the X-ray spectrum reaches $\Gamma \approx 2$). However, a steepening of the radio/X-ray correlation at that X-ray luminosity predicts a quiescent radio luminosity that is ≈0.5–0.9 dex lower than was observed in either 2003 or 2013 (for $p = 2.0$–2.3; see Figure 9). We note that empirical studies on the broadband SEDs of other hard state BHXBs suggest that the spectrum of optically thin jet synchrotron emission could (on average) follow $f_\nu \propto \nu^{-(0.7-0.8)}$ (Russell et al. 2013), from which one infers p as large as 2.6, corresponding to $q_{cool} = 1.6$. Synchrotron-cooled X-ray emission could therefore yield a slope as shallow as $m_{cool} = 0.9$. Even in this limiting case, synchrotron-cooled X-ray emission underpredicts the observed pre-outburst radio luminosities of V404 Cygni by ≈0.3 dex. Synchrotron-cooled X-rays in quiescence also appear unlikely from the radio properties of A0620−00 (Gallo et al. 2006) and XTE J1118+480 (Gallo et al. 2014, both sources at $L_X \approx 10^{-8.5} L_{Edd}$). Although, for those two sources, it is not possible to isolate the inflection point in X-ray luminosity, where the radio/X-ray correlation should steepen. A steepening of the radio/X-ray correlation in quiescence also appears to be disfavored from statistical analyses of supermassive black holes (e.g., Dong & Wu 2015).

In light of the above, we suggest two possibilities for a jet X-ray origin in quiescence: (1) the X-ray emission is SSC with synchrotron-cooled seed photons (also see, e.g., Markoff et al. 2005 for discussions on SSC from jet models); or (2) particle acceleration along the jet becomes less efficient with decreasing luminosity. In the first case, for SSC arising from an optically thin plasma, q is generally expected to be larger (i.e., less efficient)

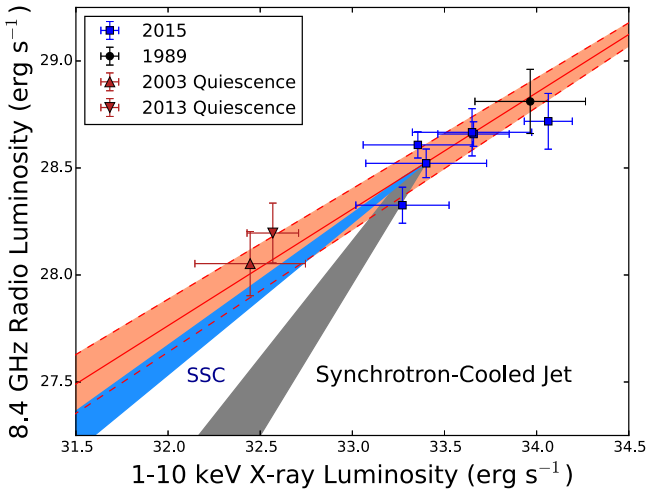

Figure 9. Radio/X-ray luminosity correlation from Figure 7, zoomed in on the 2015 data. Symbols have the same meaning as in Figure 7. The gray shaded region shows the predicted path V404 Cygni would take through the radio/X-ray plane if the X-ray spectral softening signifies a switch to synchrotron-cooled X-ray emission in quiescence, a scenario that is inconsistent with the pre-outburst radio luminosity. The light blue shaded region illustrates the path if the X-rays switch to SSC emission with synchrotron-cooled seed photons.

than the value for the mechanism that produces the source of seed photons, on account of SSC depending on the product of the photon field density and the particle density (e.g., Falcke & Biermann 1995). For simplicity, we will assume here that q will increase by one (e.g., for a conical jet without velocity gradients in the bulk flow, the particle density normalization is expected to scale linearly with $\dot{M}$; Heinz & Sunyaev 2003). In that case, the radiative efficiency of SSC (with synchrotron-cooled seed photons) for $2.0 < p < 2.3$ would be $2.0 < q_{\rm SSC,cool} < 2.3$, implying $0.6 < m_{\rm SSC,cool} < 0.7$ (or $m_{\rm SSC,cool} > 0.5$ for $p < 2.6$). Such a change in slope of the radio/X-ray correlation (i.e., $m \approx 0.5$ in the hard state to 0.6–0.7 in quiescence, for $2.0 < p < 2.3$) may not be detectable given the pre-outburst luminosity of V404 Cygni (see Figure 9).

SSC X-rays with synchrotron-cooled seed photons could also plausibly explain the softer quiescent X-ray spectrum, if the Comptonized spectrum is produced by single scatterings off an optically thin plasma.[20] To properly assess the radiative efficiency and spectral shape of SSC emission would require detailed Componization modeling, to simulate the number of scatterings, the energy distribution of the synchrotron emitting particles, and adiabatic cooling losses related to the escape rate of the highest energy particles (also see, e.g., Malzac & Belmont 2009 for relevant discussions on calculating SSC in the context of a coronal BHXB model), which we intend to address in a future paper.

For the second possibility of inefficient particle acceleration, the observed $\Gamma \approx 2$ implies (uncooled) optically thin synchrotron radiation emitted by a non-thermal population of particles with $p \approx 3$, which results in $q_{\rm thin} \approx (17/12) + (p-1)/3 = 2.1$ (e.g., Plotkin et al. 2012, and references therein). In this case, we expect a radio/X-ray correlation slope of $m_{\rm thin} = 0.7$, consistent with our prediction for SSC emission. The X-ray spectral softening during the transition into quiescence is straightforward to explain if the larger Γ is driven by a transition to optically thin synchrotron radiation emitted by a population of non-thermal electrons with $p = 3$, since $\Gamma = (p+1)/2$ for optically thin synchrotron. We cannot distinguish between SSC and inefficient particle acceleration here.

Finally, we note that at even lower luminosities ($L_{\rm X} \approx 10^{-8.5} L_{\rm Edd}$), a transition to SSC X-rays in quiescence has also been suggested from broadband modeling of two other systems—A0620−00 (Gallo et al. 2007) and XTE J1118+480 (Plotkin et al. 2015)—and also phenomenologically from the broadband spectrum of a third system, Swift J1357.2−0933 (Plotkin et al. 2016); this transition may also be accompanied by a decrease in the particle acceleration efficiency (e.g., Plotkin et al. 2015; though, see Markoff et al. 2015; Connors et al. 2016 regarding degeneracies between weak particle acceleration and radiative cooling losses). An important caveat, however, is that in the above cases the source of synchrotron seed photons is proposed to be emitted by a mildly relativistic population of electrons following a thermal distribution of energies, and not necessarily synchrotron-cooled emission from a non-thermal jet (see Shahbaz et al. 2013; Plotkin et al. 2015; Connors et al. 2016 for details).

4.3. A Tentative Size for the Compact Jet

In Section 3.2.1, we present tentative evidence for correlated radio and X-ray emission on August 5 with a 15.4 ± 4.0 minute radio lag. The best-fit correlation slopes on August 5 ($m = 0.42 \pm 0.15$; or $m = 0.59 \pm 0.17$ after removing the radio time delay) are, furthermore, consistent with an RIAF or jet origin (from SSC or weakly accelerated particles) for the X-ray emission. If this correlated variability is real, then it implies that disk/jet couplings hold on minute-long timescales, even in quiescence. Previous long simultaneous radio and X-ray observations of V404 Cygni in quiescence did not detect correlated radio and X-ray variations, most likely because our study is the first with sufficiently matched radio and X-ray sensitivities: the 2003 VLA and *Chandra* campaign (Hynes et al. 2004, 2009) was performed before the VLA upgrade, so that radio light curves were binned on ≈15–20 minute intervals; the more recent 2013 campaign (with the upgraded VLA and *NuSTAR*; Rana et al. 2016) was limited to ≈50 minute X-ray time bins due to the sensitivity of *NuSTAR*. Those two previous campaigns do, however, exclude the possibility of longer radio and X-ray time lags (up to ≈5–10 hr; the possibility of even longer lags is not constrained).

The measurement of a radio time delay opens the possibility of placing constraints on the size of the radio jet. If we denote z as the distance from the black hole along the axis of the jet, then we can approximate the X-rays as originating at $z \approx 0$ (i.e., the X-rays are emitted very close to the black hole, at a location consistent with the base of the jet), and we can define the 8.4 GHz radio emission as originating from a region located at a larger distance z_0. If information from X-ray variations propagate down the axis of the jet with a dimensionless bulk speed $\beta = v_{\rm b}/c$ (where $v_{\rm b}$ is the bulk speed and c is the speed of light), then $z_0 = \beta c \Delta t (1 - \beta \cos\theta)^{-1}$, where Δt is the radio time delay, θ is the viewing angle between the jet axis and our line of sight, and $(1 - \beta \cos\theta)$ is a correction term related to superluminal motion. By approximating θ as the orbital inclination $i = 67^{+3}_{-1}$ deg, then $\beta < 1$ places an upper limit on the jet size to $z_0 < 3.0 \pm 0.8$ au. This size limit is based only

[20] As noted by Corbel et al. (2008), the slope of $m \approx 0.5$ in the hard state could be consistent with SSC from optically thin synchrotron seed photons with $p = 2.0$–2.3, which yields $q_{\rm SSC,thin} = 2.8$ and $m_{\rm SSC,thin} \approx 0.5$. Although, such an interpretation in the low-hard state is less likely for other BHXBs, since other sources generally show steeper radio/X-ray correlation slopes.

on geometric arguments and not specific to any jet model, the only assumptions being that the X-ray flare signifies the beginning of material propagating down the jet, the adopted viewing angle, and that there is no velocity gradient in the bulk flow. However, the latter two assumptions in particular require further scrutiny. For example, VLBA observations during the 2015 outburst of V404 Cygni suggest that assuming $\theta = 67$ deg for the viewing angle might not be valid (J. C. A Miller-Jones et al. 2016, in preparation).

Despite the above approximations, the calculated $z_0 < 3.0$ au limit is consistent with a direct limit placed on V404 Cygni in quiescence, where the compact core remains unresolved in high-resolution radio observations, providing a projected angular size of <1.3 milliarcsec (Miller-Jones et al. 2008), which corresponds to a physical length $z_0 < 3.4$ au (assuming $d = 2.39$ kpc and $\theta = 67°$). If the X-ray variations are indeed propagating down the jet toward the radio photosphere, then in addition to the time delay, we expect the radio light curve to be a "smoothed" version of the X-ray light curve: the radio emitting region will have a larger physical size than the X-ray emitting one, thereby smearing the radio signal (according to the light travel time across the radio emitting region) and supressing the highest (temporal) frequency variations (see, e.g., Gleissner et al. 2004, and references therein). If we smooth our X-ray light curve with a 10-minute sliding filter[21], then the X-ray variations decrease from $F_{\rm var} = 0.28 \pm 0.03$ (see Table 5) to $F_{\rm var} = 0.23 \pm 0.03$, which is similar to the observed radio light curve from which we measure $F_{\rm var} = 0.22 \pm 0.02$. Although this is an intriguing result, further study is required. For example, if we also reduce the amplitude of the X-ray variability by $L_{\rm R}^{0.54}$ (i.e., according to the radio/X-ray luminosity correlation), then smoothing the X-ray light curve yields rms fluctuations ($F_{\rm var} = 0.15 \pm 0.03$) that are smaller than observed in the radio. Plus, the above ignores the effects of photon pileup on the *Chandra*-based $F_{\rm var}$ estimate (though these effects are expected to be small; see Appendix B).

We stress that our radio and X-ray observations on August 5 do not cover an entire flare, thereby making it difficult to understand systematics on our radio lag measurement. Thus, we present the $z_0 < 3.0 \pm 0.8$ au limit here as an example of the type of constraints that are attainable with current facilities, if one were to obtain longer stretches of strictly simultaneous radio and X-ray coverage (and measuring a time delay at $\geqslant$2 radio frequencies might provide knowledge of β, which would yield a measurement on z_0 instead of a limit[22]). So far, constraints on jet sizes are sparse, as, even at higher luminosities, we have direct constraints on the sizes of the compact, partially self-absorbed radio core for only three sources that have been resolved in the radio: GRS 1915+105 (projected size ≈25–30 au at 8.4 GHz and 8.6 kpc source distance; Dhawan et al. 2000; Reid et al. 2014), Cyg X-1 (projected size ≈28 au at 8.4 GHz and 1.86 kpc source distance; Stirling et al. 2001; Reid et al. 2011), and MAXI J1836−194 (projected size ≈60–150 au at 2.3 GHz, albeit with an uncertain distance of 4–10 kpc; Russell et al. 2015), plus the aforementioned limit on V404 Cygni in quiescence. A more precise measure for V404 Cygni would open the door to comparative studies to study how physical properties evolve from the hard state to quiescence, providing crucial constraints to inform jet models (see, e.g., Heinz 2006).

[21] The appropriate filter is jet model dependent, but it is expected to be of comparable (or smaller) length than the measured time delay. For example, for a conical geometry, one expects the size of the radio emitting region to be $z_0 \tan\phi$, where ϕ is the opening angle of the jet.

[22] We searched for a frequency dependent time delay by cross-correlating the August 5 X-ray light curve to the radio light curves at each of our four observing frequencies (from 5.2 to 11.0 GHz). Although delays were detected at all four frequencies, all were consistent with -15 ± 4 minute with no discernible trend with observing frequency, which implies that a larger range of radio frequencies should be searched, and/or that systematics related to the short time coverage are influencing our results.

5. CONCLUSIONS

We have presented a series of X-ray and radio spectra of V404 Cygni during the end of its 2015 outburst, as it transitioned back into quiescence. Even though V404 Cygni was a factor of ≈3–12 (≈2–5) more luminous in the X-ray (radio) during our campaign compared to pre-outburst, by our final observing epoch its other multiwavelength properties were similar to pre-outburst, including a soft X-ray spectrum ($\Gamma \approx 2$), modest X-ray variability ($F_{\rm var} \approx 20\%$–50%), and a flat/inverted radio spectrum. We thus conclude that V404 Cygni reached the quiescent spectral state before it settled to its minimum quiescent luminosity.

We suggest that V404 Cygni enters the quiescent spectral state at $L_{0.5-10\,{\rm keV}} \approx 3 \times 10^{33}$ erg s^{-1} (determined by the luminosity when the X-ray spectrum finishes softening to $\Gamma \approx 2$). There is no corresponding evolution in the shape of the radio spectrum, or in the slope of the radio/X-ray luminosity correlation. From the latter, we exclude the possibility that X-ray emission is dominated by a synchrotron jet in quiescence (Yuan & Cui 2005), unless the X-rays are SSC with synchrotron-cooled seed photons, or particle acceleration along the jet becomes less efficient in quiescence. From correlated X-ray and radio variability on our final observing epoch (August 5), we tentatively measure the radio emission lagging behind the X-rays by 15.4 ± 4.0 minute, which would imply a jet size $<3.0 \pm 0.8$ au (measured between the jet base and the location of the 8.4 GHz photosphere). Better multiwavelength coverage of a simultaneous X-ray and radio flare in quiescence is required.

Because of its well-constrained distance and orbital parameters, V404 Cygni is an exceptionally important source for understanding quiescent accretion flows and jets. As a long-orbital period system with a large accretion disk, V404 Cygni settles to a relatively high quiescent luminosity of $\approx 10^{33}$ erg s^{-1} (e.g., Menou et al. 1999). In the future, it will be insightful to perform a similar campaign on a shorter orbital period system, to determine if BHXBs with smaller accretion disks (and lower minimum quiescent luminosities) complete their X-ray spectral softening and re-enter the quiescent state as rapidly as V404 Cygni, and/or at a similar luminosity. Finally, as the most luminous quiescent BHXB with a well-determined distance, our improved knowledge on V404 Cygni in quiescence will help guide multiwavelength surveys to discover new (and less biased) populations of BHXBs through their quiescent radiative signatures (e.g., Jonker et al. 2011; Strader et al. 2012; Chomiuk et al. 2013; Fender et al. 2013; Torres et al. 2014; Miller-Jones et al. 2015; Tetarenko et al. 2016).

We thank the anonymous referee for constructive comments that improved this manuscript. We are especially grateful to the *Chandra*, VLA, and *Swift* teams for coordinating these observations, particularly Belinda Wilkes and Neil Gehrels for approving the *Chandra* and *Swift* observations, and especially

Scott Wolk for patiently assisting with multiple iterations of our *Chandra* observing setup. We also thank Mark Claussen, Gustaaf van Moorsel, and Heidi Medlin for their assistance with the VLA observations. We thank Arash Bahramian for helpful discussions on the X-ray decay timescale that assisted the timing of our trigger, and Thomas Russell for assistance with the radio data reduction. R.M.P. acknowledges support from Curtin University through the Peter Curran Memorial Fellowship. J.C.A.M.-J. is supported by an Australian Research Council Future Fellowship (FT140101082). G.R.S. acknowledges support from NSERC Discovery Grants. D.A. acknowledges support from the Royal Society. Support for this work was provided by the National Aeronautics and Space Administration through *Chandra* Award Number GO5-16032A issued by the *Chandra* X-ray Observatory Center, which is operated by the Smithsonian Astrophysical Observatory for and on behalf of the National Aeronautics Space Administration under contract NAS8-03060. The scientific results reported in this article are based to a significant degree on observations made by the *Chandra* X-ray Observatory. This research has made use of software provided by the *Chandra* X-ray Center (CXC) in the application packages CIAO. The National Radio Astronomy Observatory is a facility of the National Science Foundation operated under cooperative agreement by Associated Universities, Inc.

Facilities: CXO, *NuSTAR*, *Swift*, VLA.

Software: CIAO (v4.8; Fruscione et al. 2006), HEASOFT, NUSTARDAS (v1.6.0), ISIS (Houck & Denicola 2000), CASA (v4.5; McMullin et al. 2007).

APPENDIX A
ON THE COLUMN DENSITY

Here, we address a couple points regarding our best-fit column density ($N_{\rm H} = 8.4 \pm 0.2 \times 10^{21}$ cm^{-2}). First, as pointed out in the text, some studies of V404 Cygni in quiescence favor a larger column density than we do (e.g., 1.2×10^{22} cm^{-2} in Reynolds et al. 2014 and Rana et al. 2016), which we attribute to using different abundances when modelling photoelectric absorption. To illustrate this point, we refit our August 5 *Chandra* spectrum (i.e., our observation with the most counts) using Wilms et al. (2000) abundances, and we obtain $N_{\rm H} = (1.2 \pm 0.1) \times 10^{22}$ cm^{-2}. We stress that our conclusions on the X-ray spectral softening are not sensitive to which abundances are adopted (e.g., we find $\Gamma = 1.94^{+0.10}_{-0.02}$ on August 5 using Wilms et al. 2000 abundances, compared to $\Gamma = 1.99 \pm 0.04$ adopted in the text using Anders & Grevesse 1989 abundances).

Second, throughout the text, we adopt spectral parameters obtained from a joint fit, where we force a common $N_{\rm H}$ across all epochs. This decision is made because we do not see large fluctuations in $N_{\rm H}$ during our campaign. In light of the high column density observed during the first two weeks of the outburst (e.g., Motta et al. 2016; Sanchez-Fernandez et al. 2016), we present more details here to justify our choice of using a common $N_{\rm H}$. In Figure 10, we display our best-fit $N_{\rm H}$ and Γ values when we jointly fit the *Chandra* and *Swift* spectra, but allowing both $N_{\rm H}$ and Γ to vary on each epoch. There are some mild variations in $N_{\rm H}$ between epochs, but these variations are consistent with the errors (and after taking into account the expected degeneracies between $N_{\rm H}$ and Γ). We tend to obtain slightly higher best-fit $N_{\rm H}$ values on epochs before July 28 ($>10^{22}$ cm^{-2}), which could be indicative of a lingering column that did not fully dissipate until the final week of July. However, the differences pre- and post-July 28 are generally $<1\sigma$. Furthermore, July 28 is the date when we stopped using the *Chandra* HETG to mitigate pileup. Thus, the slightly higher best-fit $N_{\rm H}$ values earlier in the decay could feasibly be related to systematics caused by the poorer soft X-ray response, and we do not see overwhelming evidence for significantly varying column densities. Finally, we display a spectral fit to the August 5 *Chandra* spectrum (using Anders & Grevesse 1989 abundances) in Figure 11 to illustrate the quality of our fits.

APPENDIX B
DETAILS ON X-RAY SPECTRAL ANALYSIS AND PILEUP CORRECTIONS

Here, we expand on our discussion of the X-ray spectral analysis in Section 2.4 by describing tests regarding pileup corrections to the *Chandra* observations. One effect of pileup is energy migration, where two photons are registered as a single event with an energy (improperly) set to the total energy of both photons, which causes the observed spectrum to appear harder than the intrinsic one. By applying the Davis (2001) pileup model to the *Chandra* data during the spectral fits, we correct for this effect and recover unpiled photon indices.

One of the assumptions behind the Davis (2001) model is that the X-rays are emitted at a constant count rate. However, as described in Section 3, V404 Cygni was variable during the *Chandra* observations. To check that the variability was not strong enough to violate the assumption for constant count rate, we divided each *Chandra* observation into two to three segments, with each segment filtered over time periods when V404 Cygni displayed similar count rates (the boundaries for the count rate filters were chosen so that each segment contained a comparable number of total counts). For each epoch, we then performed a joint fit to the two to three segments by allowing the photon index Γ and the pileup grade migration parameter α to vary for each segment, but tying the best-fit column density $N_{\rm H}$ to a common value. We obtained similar best-fit photon indices for each segment, and the best-fit spectral parameters were comparable to the values obtained when we applied the pileup model to each full observation. The only exception is on July 15, where the count rate from V404 Cygni dropped to <0.03 count s^{-1} for the final 400 s of the observation (compared to an average count rate of 0.065 ± 0.004 during the rest of the observation; at no other point in that observation was the count rate <0.03 count s^{-1}). While we do not expect that change in the count rate to influence the pileup correction, it was not possible to empirically test this expectation since only eight counts were detected from V404 Cygni over those 400 s. We therefore chose to remove those 400 s from the observation. We cannot envision that this choice to err on the conservative side for the spectral fitting would impact our other results, especially considering that we had *Swift* monitoring on that date for over 19 hr, which provides additional variability information and indeed confirms that the flux level decreased shortly after the July 15 *Chandra* observation ended (see Figure 2).

Due to grade migration, photon pileup can also act to suppress the observed amplitude of X-ray flux variations. However, we do not find variability suppression to be a highly significant effect for our observations, based on the following test. We filtered our August 5 *Chandra* spectrum (i.e., our brightest and most variable observation) to include only time periods with the highest count rates (>0.5 count s^{-1}). The pileup fraction in this filtered

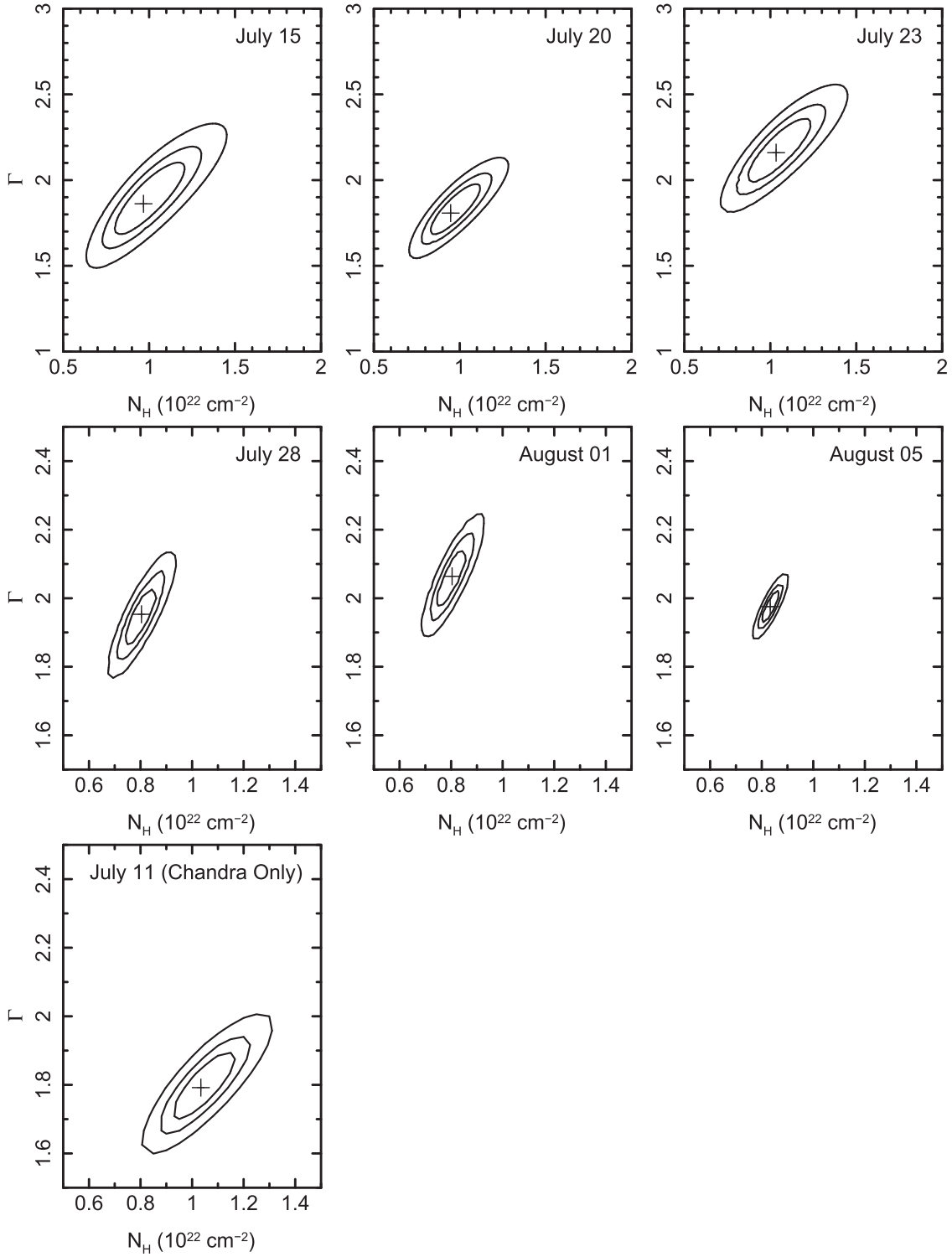

Figure 10. Confidence contour maps of joint spectral fits to the *Chandra* and *Swift* observations for the photon index (Γ) and the column density ($N_{\rm H}$), when allowing $N_{\rm H}$ to vary as a free parameter on each epoch. Contours denote 68%, 90%, and 99% confidence intervals (corresponding to changes in the Cash statistic of $\Delta C = 2.3$, 4.6, and 9.2, respectively, for two parameters of interest). The final panel for July 11 does not include *Swift* data. Note the different axis scales for the top row, and that because we allow $N_{\rm H}$ to vary during each epoch, the errors illustrated here are larger than those listed in Table 3.

spectrum remained mild at 14% (with $\alpha \approx 0.96$). Such a pileup fraction from observations with a 0.4 s frame time implies that the observed count rate is on average a factor of 0.84 smaller than the average intrinsic count rate[23] (the fractional variability will be reduced by a similar factor). We stress that the above estimate is a limit, as we only see such large count rates from ≈200–400 minutes into the August 5 observation. The suppression of variability from pileup during other less extreme X-ray flares will be less severe (including during the August 5 flare from which we estimate a radio/X-ray time delay, which peaks at a *Chandra* count rate of <0.5 count s^{-1}).

[23] See Equation (3) of http://cxc.harvard.edu/ciao/download/doc/pileup_abc.pdf.

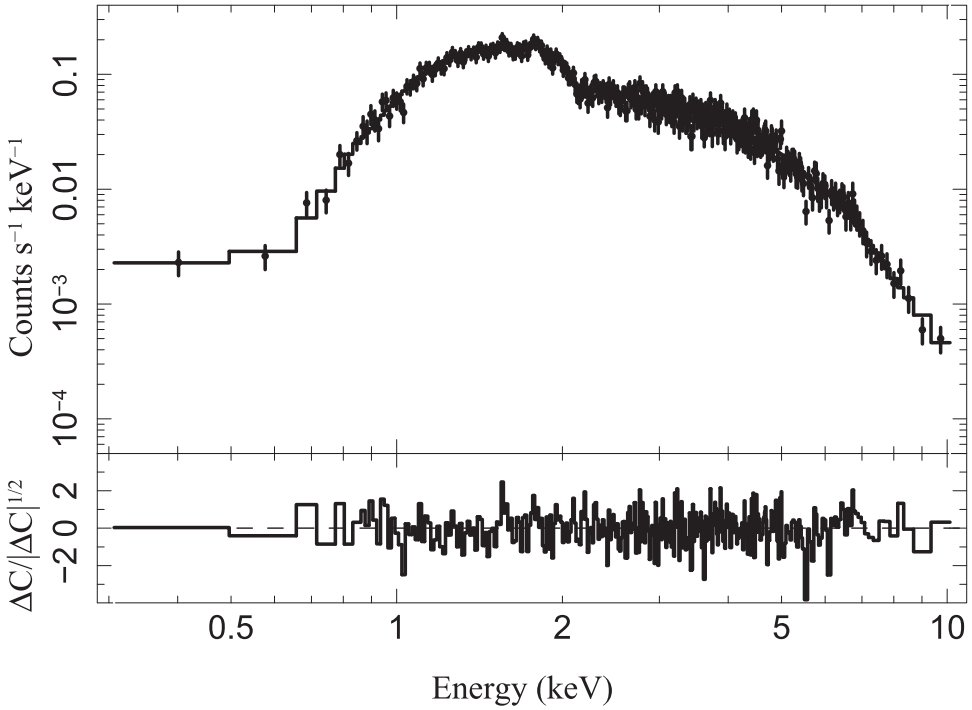

Figure 11. *Chandra* X-ray spectrum from August 5, as an example of the quality of our spectral fits.

As a final check on our pileup correction, we note that our final three observations show weak readout streaks, which are produced by photons that strike the detector while an ACIS frame is being read. Only the readout streak from the final observation (obsID 16707; August 5) is strong enough for a meaningful spectral analysis (139 net counts, opposed to $\lesssim$30 net counts in each of the other two streaks). For this final observation, we extracted a streak spectrum from 0.5 to 8.0 keV, using rectangular apertures aligned with the streak on either side of V404 Cygni. We created rmf and arf files at the location of V404 Cygni, using the tools `mkacisrmf` and `mkarf`, respectively. The effective exposure time of the streak spectrum was 358 s, which is equal to $N_{\rm frames} * N_{\rm rows} * 4 \times 10^{-5}$ s, where $N_{\rm frames}$ is the number of frames read (total exposure time/frame time = 42696 s/0.4 s), $N_{\rm row}$ is the number of rows in our streak apertures (84 rows), and 4×10^{-5} s is the readout time for each ACIS frame. We fit an absorbed power-law model, finding $N_{\rm H} = 1.0 \pm 0.4$ cm^{-2} and $\Gamma = 2.0 \pm 0.2$ when allowing $N_{\rm H}$ to vary, and $\Gamma = 1.8 \pm 0.2$ when freezing $N_{\rm H}$ to 8.4×10^{21} cm^{-2}. Thus, the streak spectrum provides consistent results to the fits performed with the Davis (2001) model (within the errors).

REFERENCES

Abramowicz, M. A., Chen, X., Kato, S., Lasota, J.-P., & Regev, O. 1995, ApJL, 438, L37
Achterberg, A., Gallant, Y. A., Kirk, J. G., & Guthmann, A. W. 2001, MNRAS, 328, 393
Anders, E., & Grevesse, N. 1989, GeCoA, 53, 197
Armas Padilla, M., Degenaar, N., Russell, D. M., & Wijnands, R. 2013, MNRAS, 428, 3083
Armas Padilla, M., Wijnands, R., Degenaar, N., et al. 2014, MNRAS, 444, 902
Asplund, M., Grevesse, N., Sauval, A. J., & Scott, P. 2009, ARA&A, 47, 481
Balucinska-Church, M., & McCammon, D. 1992, ApJ, 400, 699
Barthelmy, S. D., D'Ai, A., D'Avanzo, P., et al. 2015, GCN, 17929, 1
Beardmore, A. P., Altamirano, D., Kuulkers, E., et al. 2015a, ATel, 7736, 1
Beardmore, A. P., Page, K. L., & Kuulkers, E. 2015b, ATel, 8455, 1
Beardmore, A. P., Willingale, R., Kuulkers, E., et al. 2016, MNRAS, 462, 1847
Bell, A. R. 1978, MNRAS, 182, 147
Bell, M. E., Tzioumis, T., Uttley, P., et al. 2011, MNRAS, 411, 402
Belloni, T. M. 2010, in Lecture Notes in Physics, Vol. 794, ed. T Belloni (Berlin: Springer), 53
Bernardini, F., & Cackett, E. M. 2014, MNRAS, 439, 2771
Bernardini, F., Russell, D. M., Kolojonen, K. I. I., et al. 2016a, ApJ, 826, 149
Bernardini, F., Russell, D. M., & Lewis, F. 2016b, ATel, 8515, 1
Blandford, R. D., & Begelman, M. C. 1999, MNRAS, 303, L1
Blandford, R. D., & Königl, A. 1979, ApJ, 232, 34
Bradley, C. K., Hynes, R. I., Kong, A. K. H., et al. 2007, ApJ, 667, 427
Burrows, D. N., Hill, J. E., Nousek, J. A., et al. 2005, SSRv, 120, 165
Canizares, C. R., Davis, J. E., Dewey, D., et al. 2005, PASP, 117, 1144
Casares, J., Charles, P. A., & Naylor, T. 1992, Natur, 355, 614
Cash, W. 1979, ApJ, 228, 939
Chomiuk, L., Strader, J., Maccarone, T. J., et al. 2013, ApJ, 777, 69
Connors, R. M. T., Markoff, S., Nowak, M. A., et al. 2016, MNRAS, submitted (arXiv:1612.00953)
Corbel, S., Coriat, M., Brocksopp, C., et al. 2013, MNRAS, 428, 2500
Corbel, S., Koerding, E., & Kaaret, P. 2008, MNRAS, 389, 1697
Corbel, S., Tomsick, J. A., & Kaaret, P. 2006, ApJ, 636, 971
Davis, J. E. 2001, ApJ, 562, 575
Dhawan, V., Mirabel, I. F., & Rodríguez, L. F. 2000, ApJ, 543, 373
Dong, A. J., & Wu, Q. 2015, MNRAS, 453, 3447
Drury, L. O. 1983, RPPh, 46, 973
Edelson, R. A., & Krolik, J. H. 1988, ApJ, 333, 646
Esin, A. A., McClintock, J. E., & Narayan, R. 1997, ApJ, 489, 865
Falcke, H., & Biermann, P. L. 1995, A&A, 293, 665
Fender, R. P. 2001, MNRAS, 322, 31
Fender, R. P., Gallo, E., & Jonker, P. G. 2003, MNRAS, 343, L99
Fender, R. P., Maccarone, T. J., & Heywood, I. 2013, MNRAS, 430, 1538
Ferrigno, C., Bozzo, E., Boissay, R., Kuulkers, E., & Kretschmar, P. 2015, ATel, 7731, 1
Fruscione, A., McDowell, J. C., Allen, G. E., et al. 2006, Proc. SPIE, 6270, 62701V
Gallo, E., Fender, R. P., Miller-Jones, J. C. A., et al. 2006, MNRAS, 370, 1351
Gallo, E., Migliari, S., Markoff, S., et al. 2007, ApJ, 670, 600
Gallo, E., Miller-Jones, J. C. A., Russell, D. M., et al. 2014, MNRAS, 445, 290
Gandhi, P., Littlefair, S. P., Hardy, L. K., et al. 2016, MNRAS, 459, 554
Garmire, G. P., Bautz, M. W., Ford, P. G., Nousek, J. A., & Ricker, G. R., Jr. 2003, Proc. SPIE, 4851, 28
Gehrels, N., Chincarini, G., Giommi, P., et al. 2004, ApJ, 611, 1005
Gleissner, T., Wilms, J., Pooley, G. G., et al. 2004, A&A, 425, 1061
Han, X., & Hjellming, R. M. 1992, ApJ, 400, 304
Harrison, F. A., Craig, W. W., Christensen, F. E., et al. 2013, ApJ, 770, 103
Heinz, S. 2004, MNRAS, 355, 835

Heinz, S. 2006, ApJ, 636, 316
Heinz, S., Corrales, L., Smith, R., et al. 2016, ApJ, 825, 15
Heinz, S., & Sunyaev, R. A. 2003, MNRAS, 343, L59
Hjellming, R. M., & Johnston, K. J. 1988, ApJ, 328, 600
Homan, J., Fridriksson, J. K., Jonker, P. G., et al. 2013, ApJ, 775, 9
Houck, J. C., & Denicola, L. A. 2000, in ASP Conf. Ser. 216, Astronomical Data Analysis Software and Systems IX, ed. N. Manset, C. Veillet, & D. Crabtree (San Francisco, CA: ASP), 591
Hynes, R. I., Bradley, C. K., Rupen, M., et al. 2009, MNRAS, 399, 2239
Hynes, R. I., Charles, P. A., Garcia, M. R., et al. 2004, ApJL, 611, L125
Ichimaru, S. 1977, ApJ, 214, 840
Jenke, P. A., Wilson-Hodge, C. A., Homan, J., et al. 2016, ApJ, 826, 37
Jonker, P. G., Bassa, C. G., Nelemans, G., et al. 2011, ApJS, 194, 18
Jonker, P. G., Miller-Jones, J., Homan, J., et al. 2010, MNRAS, 401, 1255
Jonker, P. G., Miller-Jones, J. C. A., Homan, J., et al. 2012, MNRAS, 423, 3308
Kalemci, E., Tomsick, J. A., Buxton, M. M., et al. 2005, ApJ, 622, 508
Kelly, B. C. 2007, ApJ, 665, 1489
Khargharia, J., Froning, C. S., & Robinson, E. L. 2010, ApJ, 716, 1105
Kimura, M., Isogai, K., Kato, T., et al. 2016, Natur, 529, 54
King, A. L., Miller, J. M., Raymond, J., Reynolds, M. T., & Morningstar, W. 2015, ApJL, 813, L37
Kong, A. K. H., McClintock, J. E., Garcia, M. R., Murray, S. S., & Barret, D. 2002, ApJ, 570, 277
Kuulkers, E., Motta, S., Kajava, J., et al. 2015, ATel, 7647, 1
Lehar, J., Hewitt, J. N., Burke, B. F., & Roberts, D. H. 1992, ApJ, 384, 453
Malzac, J. 2016, AN, 337, 391
Malzac, J., & Belmont, R. 2009, MNRAS, 392, 570
Markoff, S., Nowak, M., Corbel, S., Fender, R., & Falcke, H. 2003, A&A, 397, 645
Markoff, S., Nowak, M. A., Gallo, E., et al. 2015, ApJL, 812, L25
Markoff, S., Nowak, M. A., & Wilms, J. 2005, ApJ, 635, 1203
Martí, J., Luque-Escamilla, P. L., & García-Hernández, M. T. 2016, A&A, 586, A58
Martin-Carrillo, A., Murphy, D., Hanlon, L., et al. 2015, ATel, 7729, 1
McMullin, J. P., Waters, B., Schiebel, D., Young, W., & Golap, K. 2007, in ASP Conf. Ser. 376, Astronomical Data Analysis Software and Systems XVI, ed. R. A. Shaw, F. Hill, & D. J. Bell (San Francisco, CA: ASP), 127
Menou, K., Esin, A. A., Narayan, R., et al. 1999, ApJ, 520, 276
Merloni, A., Heinz, S., & di Matteo, T. 2003, MNRAS, 345, 1057
Miller, J. M., Homan, J., Steeghs, D., et al. 2006, ApJ, 653, 525
Miller-Jones, J. C. A., Gallo, E., Rupen, M. P., et al. 2008, MNRAS, 388, 1751
Miller-Jones, J. C. A., Jonker, P. G., Dhawan, V., et al. 2009, ApJL, 706, L230
Miller-Jones, J. C. A., Strader, J., Heinke, C. O., et al. 2015, MNRAS, 453, 3918
Mooley, K., Fender, R., Anderson, G., et al. 2015, ATel, 7658, 1
Motta, S., Beardmore, A., Oates, S., et al. 2015, ATel, 7665, 1
Motta, S. E., Kajava, J. J. E., Sánchez-Fernández, C., Giustini, M., & Kuulkers, E. 2016, arXiv:1607.02255
Muñoz-Darias, T., Casares, J., Mata Sánchez, D., et al. 2016, Natur, 534, 75
Narayan, R., Barret, D., & McClintock, J. E. 1997, ApJ, 482, 448
Narayan, R., & Yi, I. 1994, ApJL, 428, L13
Narayan, R., & Yi, I. 1995, ApJ, 444, 231
Negoro, H., Matsumitsu, T., Mihara, T., et al. 2015, ATel, 7646, 1
Niedźwiecki, A., Xie, F.-G., & Stępnik, A. 2014, MNRAS, 443, 1733
Perley, R. A., & Butler, B. J. 2013, ApJS, 204, 19
Plotkin, R. M., Gallo, E., & Jonker, P. G. 2013, ApJ, 773, 59
Plotkin, R. M., Gallo, E., Jonker, P. G., et al. 2016, MNRAS, 456, 2707
Plotkin, R. M., Gallo, E., Markoff, S., et al. 2015, MNRAS, 446, 4098
Plotkin, R. M., Markoff, S., Kelly, B. C., Körding, E., & Anderson, S. F. 2012, MNRAS, 419, 267
Poutanen, J., & Veledina, A. 2014, SSRv, 183, 61
Rana, V., Loh, A., Corbel, S., et al. 2016, ApJ, 821, 103
Ratti, E. M., Jonker, P. G., Miller-Jones, J. C. A., et al. 2012, MNRAS, 423, 2656
Reid, M. J., McClintock, J. E., Narayan, R., et al. 2011, ApJ, 742, 83
Reid, M. J., McClintock, J. E., Steiner, J. F., et al. 2014, ApJ, 796, 2
Reis, R. C., Fabian, A. C., & Miller, J. M. 2010, MNRAS, 402, 836
Remillard, R. A., & McClintock, J. E. 2006, ARA&A, 44, 49
Reynolds, M. T., & Miller, J. M. 2011, ApJL, 734, L17
Reynolds, M. T., Reis, R. C., Miller, J. M., Cackett, E. M., & Degenaar, N. 2014, MNRAS, 441, 3656
Rodriguez, J., Cadolle Bel, M., Alfonso-Garzón, J., et al. 2015, A&A, 581, L9
Roques, J.-P., Jourdain, E., Bazzano, A., et al. 2015, ApJL, 813, L22
Russell, D. M., Markoff, S., Casella, P., et al. 2013, MNRAS, 429, 815
Russell, T. D., Miller-Jones, J. C. A., Curran, P. A., et al. 2015, MNRAS, 450, 1745
Sanchez-Fernandez, C., Kajava, J. J. E., Motta, S. E., & Kuulkers, E. 2016, arXiv:1608.08802
Shahbaz, T., Ringwald, F. A., Bunn, J. C., et al. 1994, MNRAS, 271, L10
Shahbaz, T., Russell, D. M., Zurita, C., et al. 2013, MNRAS, 434, 2696
Shakura, N. I., & Sunyaev, R. A. 1973, A&A, 24, 337
Sivakoff, G., Bahramian, A., Altamirano, D., Miller-Jones, J., & Russell, D. 2015a, ATel, 7763, 1
Sivakoff, G. R., Bahramian, A., Altamirano, D., et al. 2015b, ATel, 7959, 1
Sobolewska, M. A., Papadakis, I. E., Done, C., & Malzac, J. 2011, MNRAS, 417, 280
Stirling, A. M., Spencer, R. E., de la Force, C. J., et al. 2001, MNRAS, 327, 1273
Strader, J., Chomiuk, L., Maccarone, T. J., Miller-Jones, J. C. A., & Seth, A. C. 2012, Natur, 490, 71
Tetarenko, A., Sivakoff, G. R., Bremer, M., et al. 2015a, ATel, 7740, 1
Tetarenko, A., Sivakoff, G. R., Gurwell, M. A., et al. 2015b, ATel, 7661, 1
Tetarenko, A., Sivakoff, G. R., Young, K., Wouterloot, J. G. A., & Miller-Jones, J. C. 2015c, ATel, 7708, 1
Tetarenko, B. E., Bahramian, A., Arnason, R. M., et al. 2016, ApJ, 825, 10
Tomsick, J. A., Corbel, S., & Kaaret, P. 2001, ApJ, 563, 229
Tomsick, J. A., Kalemci, E., & Kaaret, P. 2004, ApJ, 601, 439
Tomsick, J. A., Walton, D., Clavel, M., Lansbury, G., & Stern, D. 2015, ATel, 8466
Tomsick, J. A., Yamaoka, K., Corbel, S., et al. 2009, ApJL, 707, L87
Torres, M. A. P., Jonker, P. G., Britt, C. T., et al. 2014, MNRAS, 440, 365
Trushkin, S. A., Nizhelskij, N. A., & Tsybulev, P. G. 2015, ATel, 7716, 1
Uttley, P., Wilkinson, T., Cassatella, P., et al. 2011, MNRAS, 414, L60
Vasilopoulos, G., & Petropoulou, M. 2016, MNRAS, 455, 4426
Vaughan, S., Edelson, R., Warwick, R. S., & Uttley, P. 2003, MNRAS, 345, 1271
Walton, D., Harrison, F., Forster, K., et al. 2015, ATel, 7752, 1
Walton, D. J., Mooley, K., King, A. L., et al. 2016, arXiv:1609.01293
Wilms, J., Allen, A., & McCray, R. 2000, ApJ, 542, 914
Wu, Q., & Gu, M. 2008, ApJ, 682, 212
Xie, F.-G., Yang, Q.-X., & Ma, R. 2014, MNRAS, 442, L110
Yan, M., Sadeghpour, H. R., & Dalgarno, A. 1998, ApJ, 496, 1044
Yang, Q.-X., Xie, F.-G., Yuan, F., et al. 2015, MNRAS, 447, 1692
Younes, G. 2015, GCN, 17932, 1
Yuan, F., & Cui, W. 2005, ApJ, 629, 408
Yuan, F., & Narayan, R. 2014, ARA&A, 52, 529